SEGMENTED CONTROL OF ELECTROSTATICALLY ACTUATED BIMORPH MICROMIRRORS

THESIS

Kullen W. Waggoner, Captain, USAF

AFIT-ENG-MS-18-M-065

DEPARTMENT OF THE AIR FORCE
AIR UNIVERSITY

AIR FORCE INSTITUTE OF TECHNOLOGY

Wright-Patterson Air Force Base, Ohio

PATENT PENDING

This material contains information that is work for provisional patent application S/N 62/587.

AFIT-ENG-MS-18-M-065

SEGMENTED CONTROL OF ELECTROSTATICALLY ACTUATED BIMORPH MICROMIRRORS

THESIS

Presented to the Faculty

Department of Electrical and Computer Engineering

Graduate School of Engineering and Management

Air Force Institute of Technology

Air University

Air Education and Training Command

In Partial Fulfillment of the Requirements for the

Degree of Master of Science in Electrical Engineering

Kullen W. Waggoner, BSE

Captain, USAF

March 2018

AFIT-ENG-MS-18-M-065

SEGMENTED CONTROL OF ELECTROSTATICALLY ACTUATED BIMORPH MICROMIRRORS

Kullen W. Waggoner, BSE

Captain, USAF

Committee Membership:

Capt Robert A. Lake, PhD, USAF
Chair

Maj Tod Laurvick, PhD, USAF
Member

Dr. LaVern A. Starman, PhD
Member

AFIT-ENG-MS-18-M-065

Abstract

Electrostatic actuating bimorph beams are a MEMS device that can be used to control arrays of small micromirrors for optical beam scanning. Previous research has demonstrated that creating high-angle deflection using long repeating arms of bimorph beams is possible. The current devices lack precise control and measurement of the mirror deflection. A solution to improve control and measurement is by using segmented bias channels to control separate portions of the actuation arm. The amount of mirror deflection will vary depending on which segments of the arm are actuated. This thesis discusses the results of FEA modeling and testing.

Acknowledgments

I would like to express my sincere appreciation to my faculty advisor, Capt Robert Lake, for his guidance and support throughout the course of this thesis effort. The insight and experience was certainly appreciated. I would, also, like to thank my family and fiancé for support throughout class and thesis work.

Kullen W. Waggoner

Table of Contents

List of Figures

List of Tables

List of Acronyms

AFIT	Air Force Institute of Technology
AFRL	Air Force Research Lab
CAD	Computer-Aided Design
CVD	Chemical Vapor Deposition
DLP	Digital Light Processing
DMD	Digital Micromirror Display
FEA	Finite Element Analysis
IBM	International Business Machines
IC	Integrated Circuits
LPCVD	Low-Pressure Chemical Vapor Deposition
MEMS	Micro-Electro-Mechanical Systems
MOEMS	Micro-Opto-Electro-Mechanical Systems
MUMPs	Multi-User MEMS Process
NEMS	Nano-Electro-Mechanical Systems
PECVD	Plasma Enhanced Chemical Vapor Deposition
RIE	Reactive Ion Etching

SEGMENTED CONTROL OF ELECTROSTATICALLY ACTUATED BIMORPH MICROMIRRORS

1. Introduction

Microelectromechanical systems (MEMS) are extremely small devices that are used as actuators or sensors. MEMS have a great range of advantages including being extremely low-power, small, and light-weight. Because of these advantages, there is motivation by the U.S. Air Force to find new MEMS applications for aerospace vehicles and to replace legacy heavy and bulky components with MEMS type designs. One such possible application is as a large angle beam-steering device. A beam steering device is a device that has actuators to control a mirror. A laser or some other source of light incident onto the mirror can then be reflected in any direction by moving the mirrors with the actuators. Current aerospace vehicle beam-steering devices often use a large gimbal system with electric motors to control the mirror.

There are commercial MEMS micromirror beam-steering arrays currently offered on the market. Most notably, the Digital Mirror Device (DMD) by Texas Instruments which is used in many video projectors. Beam-steering arrays use a grid of micromirrors to control an incident beam and control the direction of the reflected beams. Current limitations in commercial micromirror array devices result in a reduction in their applicability to other fields. These limitations include insufficient maximum angle of beam-steering and limited fidelity of control of the beam. The Air Force Research Lab (AFRL) and the Air Force Institute of Technology (AFIT) have recently worked on a new device to overcome these limitations. The device uses a serpentine bimorph structure connected to a central platform to provide a large angle deflection. The actuation method of the micromirrors is often accomplished through electrostatic actuation

but may also be accomplished by electrothermal or some other actuation scheme. Electrostatic actuation is preferred for its fast response rate and reliability. However, a major limitation of electrostatic actuation is that they exhibit a phenomenon called pull-in. Because of pull-in, only a limited range of deflection values for an actuator have a stable static solution. This research looks at using a segmented control scheme to increase the available stable solutions for a bimorph micromirror controlled by electrostatic actuation.

2. Background

The following chapter provides details from a review of applicable literature for background on the segmented operation of MEMS beam-steering devices. This section goes into detail on the fabrication techniques used, applicable physics principles, modeling techniques, and previous work that is related to this current research.

2.1 MEMS Overview

MEMS are a category of devices that use small-scale electrical and mechanical component interactions to accomplish a desired purpose. They typically have feature sizes on the μm scale [1]. This field developed out of the microelectronic and semiconductor industry by adapting the micro-scale semiconductor manufacturing techniques from creating electronics to building devices that take advantage of mechanical properties of the materials. The following sections detail several available techniques. There are several subsets of MEMS currently, MEMS that are for optical application are microoptoelectromechanical systems (MOEMS), MEMS for radio frequency (RF) applications are called RF MEMS, and when components have sub-micron feature sizes are often referred to as nanoelectromechanical system (NEMS) [1].

2.1.1 MEMs History

The concept of making smaller and smaller small electro-mechanical devices has been a goal of many researchers ever since Richard Feynman published his famous paper *There's Plenty of Room at the Bottom* [2]. Fabrication processes that were developed for the manufacturing of microelectronics were adapted to create extremely small electro-mechanical devices for a variety of consumer applications. One of the first major commercial success in which MEMS were found to be better than other available options was in the use for micro-

machined inkjet print heads by Hewlett Packard and International Business Machines (IBM) in the 1970s [3], [4]. Research into MEMS continued and the next major application was in the use of accelerometers for vehicle airbags. MEMS accelerometer sensors (Figure 1) could be made inexpensively and rugged enough to detect and respond to vehicle collision. The accelerometer detects the large acceleration using a fixed mass and spring system and sends signal to the airbag control unit to inflate the airbags [5].

Figure 1: BOSCH high-g accelerometer for vehicle airbag system from 1990s [5].

Additional research by Texas Instruments (TI) found optical applications for MEMS. In 1987, TI built and tested the first version of what would become the Digital Micromirror DMD [6]. This device was an array of micromirrors that each act as a pixel to reflect a light source onto a screen (Figure 2). It is still used as a critical component of many Digital Light Processing (DLP) projectors such as those used in movie theaters. The device functions by each mirror rotating to either the pixel ON or pixel OFF position. Electrostatic actuation allows it to function extremely quickly in order to create frame rates of up to 16 milliseconds [6]. As shown in Figure 3, the DMD features multiple layers of micro-machined materiel to create the electrode, springs, hinges, and mirror platform [7].

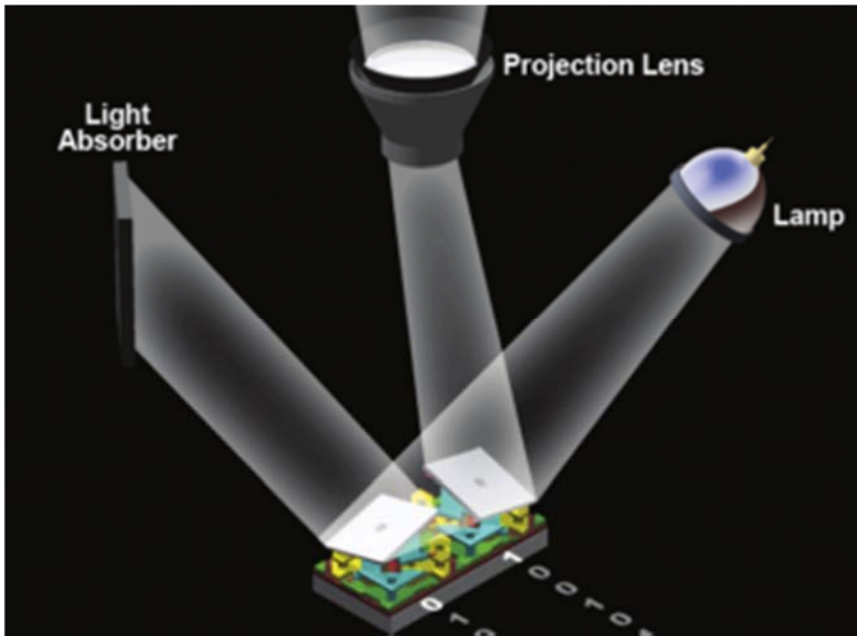

Figure 2: Texas Instruments Digital Mirror Device light beam diagram showing one pixel in ON position and one in OFF position [6].

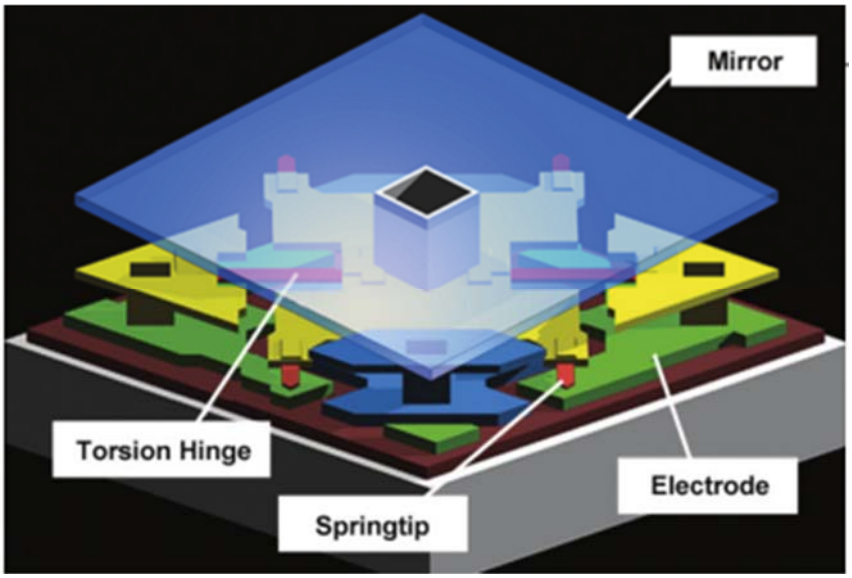

Figure 3: 3D cross-section rendering of Texas Instruments Digital Mirror Device diagram showing each layer from substrate up to mirror [6]

2.1.2 MEMS Uses

MEMS primary purpose is as a transducer. Transducers are devices that convert one form of energy to another. Transducers are divided into two categories: sensors and actuators

(Figure 4). Sensors take energy often in the form of mechanical but could be any type (optical, thermal, etc.) and converts it to an electrical voltage signal to measure a physical quantity. Actuators do the opposite, they take an electrical voltage signal and convert it to a mechanical or other type of energy to move a physical being or to cause some other desired effect [8][9][10].

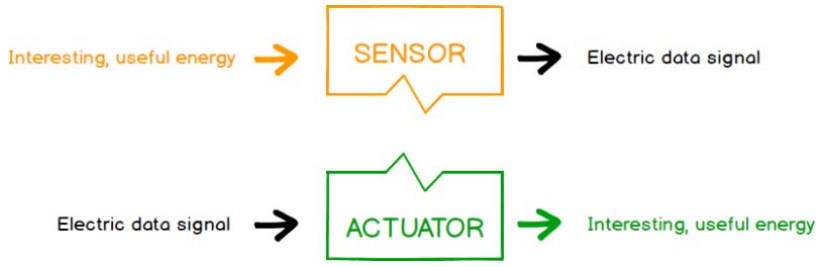

Figure 4: Block diagram showing two types of transducers: sensors and actuators. It shows basic functionality of the exchange of energy from useful energy to a data signal and back [8].

Examples of MEMS sensors and actuators are vibration sensors (Figure 5) for seismic activity and electrostatic motors (Figure 6), respectively [11], [12].

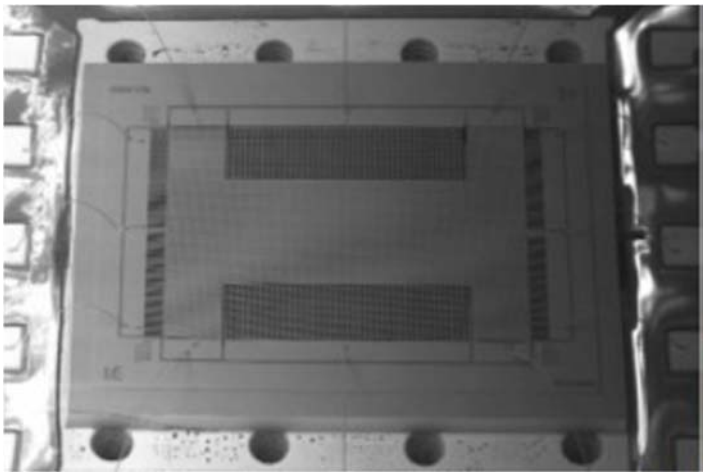

Figure 5: SEM image of an a vibrational seismic MEMS sensor [11].

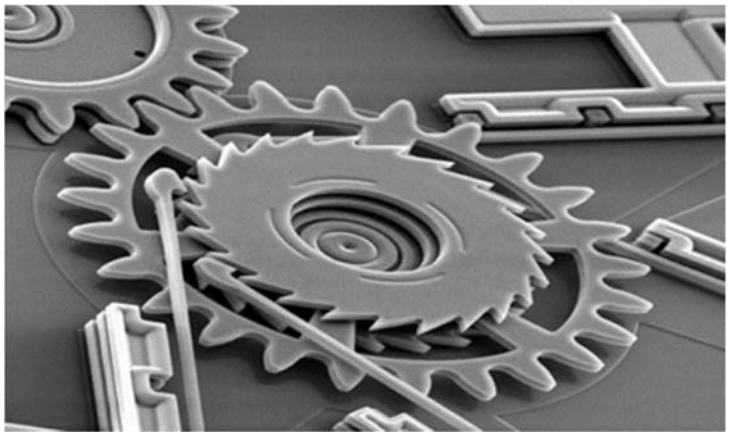

Figure 6: SEM Image of an example of an electrostatic rotational MEMS actuator [4].

2.1.3 Advantages of MEMS

The use of MEMS has brought significant advantages as compared to previous technologies. Major advantages of MEMS include but are not limited to being extremely small, lightweight, low power, and inexpensive. Most of these advantages are a direct result of their size and scaling laws for different physical parameters [13]. The small size and weight make MEMS attractive devices for aerospace applications where size and weight constraints are critical [14]. MEMS can often be a less expensive alternative for many applications. This is because MEMS are able to take advantage of economies of scale for when large chip batches are created using a single design similar to the advantages used by integrated circuit manufacturers [15].

2.2 MEMs Materials

MEMS manufacturing involves the patterning and machining of various layers of materials that include conductors, semi-conductors, and insulators. The mechanical and electrical properties of these materials are adjusted as required and used to create the various structures and electrical circuits necessary for the MEMS devices to function.

2.2.1 Conductors, semi-conductors, and insulators

Whether a material is a conductor, semi-conductor, or insulator depends on the location of the electrons within the atomic energy bands and ability to move about those bands. Conductors are materials such that either the outermost (valence) band is not fully occupied or the filled band overlaps with an empty conduction band. In an insulator, there is a large gap between the valence band and the conduction band. Finally, for semi-conductors a bandgap exists between the valence band and the conduction but it is small as compared to the insulator band gap. Figure 7 shows a visual representation of the differences between the conduction and valence bands for insulators, semiconductors and conductors. An example of a band gap for GaAs, a common semiconductor material is 1.4 eV [16].

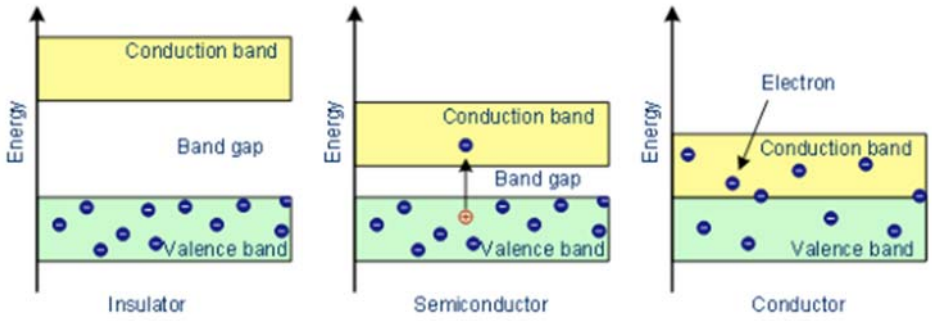

Figure 7: Band gap diagram showing valence and conduction bands for insulators, semiconductors, and conductors [17].

2.2.2 Important Materials for MEMS

MEMS use a variety of different conductors, semi-conductors, and insulators. A few examples of common materials are single crystalline silicon, poly-crystalline silicon, silicon oxide, silicon nitride, and gold [18]. The following paragraphs provide information of electronic, material, and chemical properties of these important materials.

2.2.3.1 Single-Crystal silicon

Silicon is the most common semiconductor and forms a diamond crystal cubic structure (Figure 8). This type of structure is described as two interpenetrating face center cubic structures [19]. Single-crystal silicon is grown in ingots and sliced into thin wafers (usually less than 1 mm) of varying diameters. It has a band gap of 1.12 eV at 300K. Most semiconductors and MEMS are based on a silicon wafer or a wafer of another semiconductor material. After all layers are deposited and patterned, the wafer is usually diced into many separate devices [16].

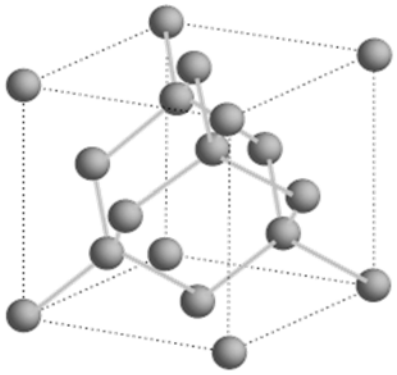

Figure 8: Diamond cubic crystal structure of silicon [19].

2.2.3.2 Poly-crystalline silicon

Poly-crystalline silicon (Figure 9) also known as polysilicon is a form of crystalline silicon. It is pure silicon and it has the same lattice structure as single-crystal silicon. The difference between single-crystal and polysilicon is that polysilicon is composed of many different small crystal domains that point in all directions. The individual crystals are joined to each other at several grain boundaries. Because of the various small crystal structures, polysilicon has a less homogenous appearance[13]. Because it is difficult to deposit single-crystal silicon onto a wafer in a thin layer to be patterned, polysilicon is often used as a deposited layer for structural layers for MEMS because it can be deposited using chemical vapor

deposition (CVD) techniques[18]. Like single-crystal silicon, polysilicon can be doped with both N and P type dopants to adjust its electronic properties.

Table 1: Selected mechanical properties for PolyMUMPS polysilicon layers from design handbook [18].

Mechanical Property	Value
Young's Modulus	158 +/- 10 GPa
Poisson's Ratio	0.22 +/- 0.01
Fracture Strength	1.21 +/- 0.8 to 1.65 +/- 0.28 GPa*

*Fracture Strength is dependent on specimen size, smaller specimens have higher strength

Mechanical properties for polysilicon can vary depending on the parameters in which it was deposited. For PolyMUMPS, the process that is used for this research, the measured mechanical properties from MEMSCAP are provided in Table 1[18] and Appendix A.

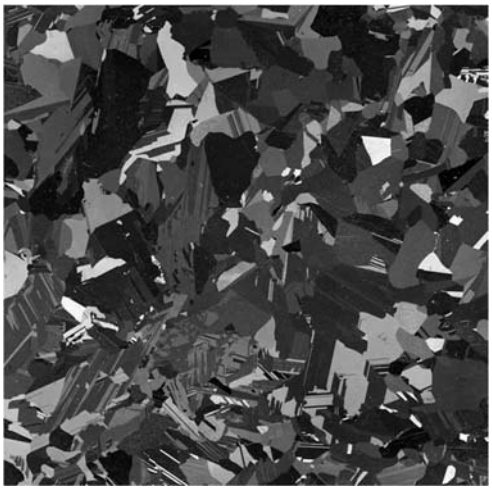

Figure 9: Image of a 10cm x10cm polysilicon wafer. This wafer was textured so that the grains show up as light and dark [20].

2.2.3.3 Silicon Dioxide

Silicon dioxide (SiO_2) is the native oxide of silicon when it is exposed to oxygen. It acts as an insulator and dielectric with an energy band gap of 8.9 eV and a dielectric constant of 3.7-3.9 [21]. It is often used in MEMS as a sacrificial layer or a layer that is deposited with the

ultimate intention of removing through an etch process to allow certain portions of a device to be able to move freely. Silicon dioxide can be grown on the surface of silicon or it can be deposited through CVD [18].

2.2.3.4 Silicon Nitride

Silicon nitride (Si_3N_4) is an insulator and a dielectric materiel that is used in MEMS. It can be used as a passivation layer covering a wafer because of its insulating properties and resistance to oxidation. It can also be used as part of the device layers itself because of its high strength. Table 2 provides relevant properties of silicon nitride [22].

Table 2: Selected properties for LPCVD silicon nitride [22].

Property	Value
Young's Modulus	385 GPa
Poisson's Ratio	0.27
Resistivity	$10^{16}\,\Omega - cm$
Coefficient of Thermal Expansion	$1.6 * 10^{-6}\ K^{-1}$

2.2.3.5 Metal

Many different types of metals are used in MEMS. They are used for a variety of different reasons including thin film conducting layers, optical layers, and structural layers. Metals are conductors and therefore have low resistance. Gold is a common layer and will be discussed in this research because it is used in the PolyMUMPS process [13], [18].

2.3 Fabrication

The following sections describe microfabrication techniques for the manufacture of MEMS. Techniques that are highlighted are those that were used for the fabrication of devices for this research effort.

2.3.1 Photolithography

Photolithography is a critical part of the MEMS fabrication process. It is often the most complicated and expensive process in micro and nanoscale fabrication [23]. The purpose of photolithography is to transfer a design pattern from a mask to a photo-resist covered wafer to control the subsequent etch or deposition process. It is a very useful process because it allows a single mask to be created that can replicated to create a great number of devices. The photolithography process (Figure 10) consists of coating a wafer with a photoresist such as SU-8 or 1818 and using a mask and an optical source. The mask is placed over the photoresist covered wafer and blocks the light from the optical source from reaching certain areas of the photoresist. Areas of photoresist that are exposed to light will react differently than those not exposed, transferring the pattern from the mask to the photoresist on the wafer.

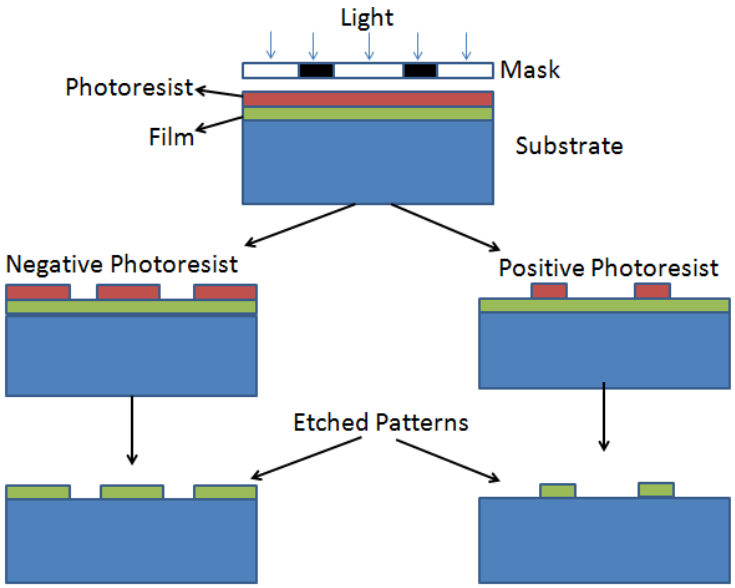

Figure 10: Diagram showing steps of photolithography and etch process for positive and negative photoresists. The first step is exposing the photoresist to the mask pattern. It is

followed by developing the photoresist, and finally, etching exposed device layer and removing remaining photoresist [24].

To accomplish this process, the design with all the required layers are designed in a computer aided drafting (CAD) program. For the designs of this project, MEMS L-Edit v8.3 was used. Once all layers of the device have been finalized, the design file is used to create masks. The total number of masks required for a fabrication will depend on the design because each mask only represents one device layer. Fabrication of commercial microelectronics can require over 20 different masks [23].

Masks are made based on the category of photoresist. The two categories of photoresist are positive and negative photoresists. This means that for positive photoresist, areas of the photoresist that are exposed to the optical source become more soluble and the areas that are not exposed will remain on the wafer. The reverse is true for negative photoresist. In negative photoresists, areas exposed to the light become less soluble to the developing agent because the polymers become crosslinked [23]. When the photoresist is developed, unwanted areas of the photoresist is removed exposing areas of the underlying device layer for removal. The exposed areas of the device layer are then able to be removed through any of several etching processes such as wet etching or reactive ion etching (RIE). Once the etching is complete, the remaining photoresist is removed and the resulting device layer is a replication of the mask layer [15].

2.3.2 Surface Micromachining

Surface micromaching is the process of additive manufacturing of patterned layers onto a wafer. In other words, it is the process of adding layers of materials, as both structural and sacrificial layer, in different geometries to form a device. Combinations of structural and sacrificial layers are typically polysilicon/silicon dioxide or metal/photoresist. It is contrasted with bulk micromaching which involves removing layers of the substrate. Figure 11 shows a

comparison of making a similar cantilever beam with both bulk and surface micromaching. The first references of surface micromaching date to the 1960s with the fabrication of resonating-gate MOS devices [10]. Surface micromaching steps can be used to form both movable and non-movable parts of a MEMS device. To form a movable part, a sacrificial oxide such a phospho-silicate glass (PSG) is layered onto a wafer, then a device layer such as polysilicon is deposited onto the PSG. After all subsequent layers have been added, the PSG is removed leaving the polysilicon certain degrees of freedom to move [10]. There are many different processes that can be used in surface micromaching. The following sections discuss a few of the major techniques that were used in fabrication for this research effort.

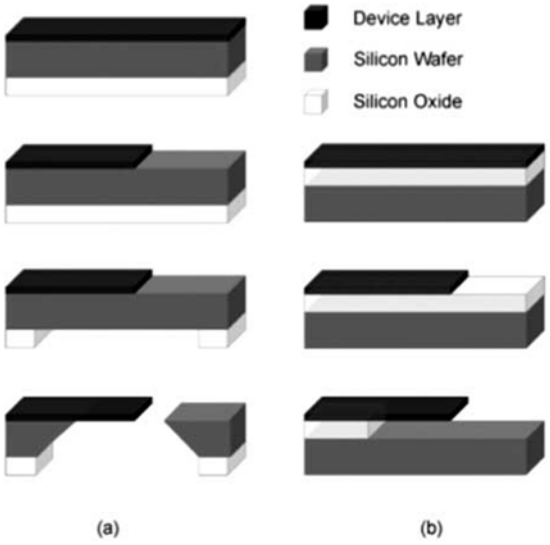

Figure 11: Diagram providing a comparison of two micromaching techniques to form a cantilever beam (a) bulk micromachining which removes portions of the substrate and (b) surface micromaching which patterns and removes portions of the deposited layers [25].

2.3.2.1 Metal Evaporation

Metal evaporation was one of the earliest methods of deposition for the semiconductor industry [23]. It is still used in many integrated circuits (IC) and MEMS processes although it has been replaced by other methods such as sputtering and electroplating because evaporation

has poor step coverage and difficulty depositing a well-controlled alloy. Figure 12 provides a diagram of a high-vacuum evaporation chamber showing to deposition of a metal. Metal evaporation functions by placing the sample wafer in a chamber, taking the chamber to a high vacuum, then the plating material or target is placed in the evaporator. The evaporator is a crucible that gets to very high temperatures to melt the target metal and allow it to evaporate. The material then vaporizes and collects on the sample wafer creating the thin film[23].

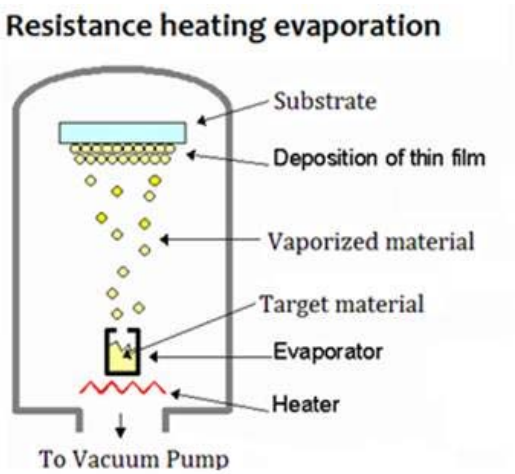

Figure 12: Diagram showing the deposition of a metal layer using evaporation. The target material evaporates and coats the substrate above[26]

2.3.2.2 Chemical Vapor Deposition (CVD)

CVD is a process that uses a chemical reaction to deposit a thin film. It is often preferred to physical deposition methods such as sputtering and evaporation for semiconductor and insulating materials [23]. The basic process of CVD is that a gaseous reactant species passes into a reaction chamber containing the wafer. A chemical reaction occurs, often a decomposition reaction which leaves a thin film on the wafer. One specific type of CVD is Low Pressure Chemical Vapor Deposition (LPCVD). There are two major types of LPCVD systems, the first is cold wall and the second is hot wall systems. Figure 13 shows a horizontal hot wall system LPCVD system. It functions by filling the deposition chamber with an inert gas such as N_2, then

the vacuum pump will pump the deposition chamber down to a medium vacuum. The heating coils then heat up the side walls and then the gaseous reactant fill the deposition chamber. The deposition then proceeds for the required amount of time for the desired thickness of coverage. Afterwards, the chamber is then filled again with a non-reactant species, brought to atmospheric pressure and the wafers are removed [23]. For silicon deposition, the most common reaction is provided in equation (1).

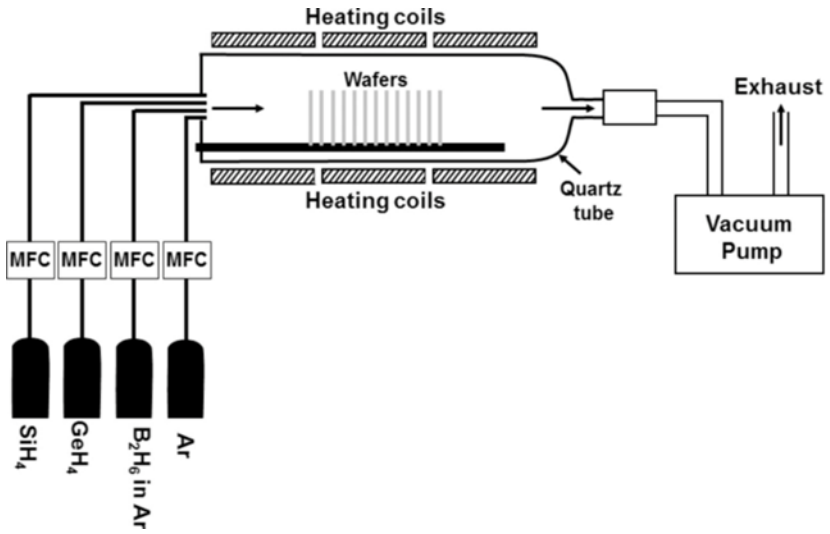

Figure 13: A hot wall LPCVD horizontal deposition system. This shows the ability to put four different types of gaseous reactants into the chamber. For polysilicon deposition SiH_4 is used. [27]

$$SiH_{4(g)} \rightarrow Si_{(s)} + 2H_{2(g)} \quad (1)$$

An additional type of CVD is Plasma-Enhanced Chemical Vapor Deposition (PECVD). PECVD uses a RF source to create a plasma that creates ion bombardment that adds necessary energy for the chemical reactions to occur for film deposition. It has the advantages that PECVD can operate at lower temperatures than other CVD techniques and still obtain an even coating [23]. As shown in Figure 14, in the deposition chamber, the gaseous reactants are input, then the

RF energy creates a plasma between the cathode and anode regions. This allows the requisite chemical reaction to take place for the thin film to be deposited [23].

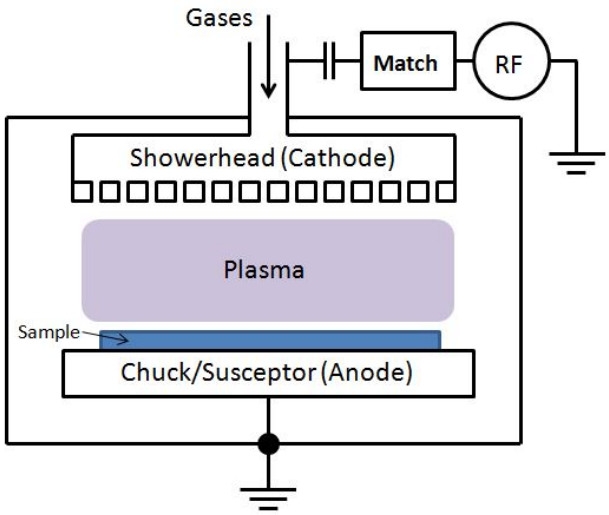

Figure 14: Cold wall PECVD chamber showing introduction of gaseous reactants and the plasma formation above the sample wafer. [28]

2.3.3 Bulk Micromaching and Etching

Bulk micromaching is similar to surface micromaching except that instead of adding layers on top of a substrate, material from the wafer is selectively removed to create trenches, holes, or other structures [29]. Bulk micromachining can be used in conjunction with surface micromachining to create more complex devices. To remove the material a variety of etching techniques can be employed including wet, vapor, and plasma. Vapor and plasma etching are commonly referred to as 'dry' because it does not involve submerging or exposing the wafer to a liquid etchant such a Potassium Hydroxide (KOH). The type of etchant used will depend on constraints of the device and the desired etch profile. Some etching techniques will etch all directions of the wafer evenly, this is called isotropic etching and some will etch in one direction more than others, this is referred to as anisotropic etching [29][30].

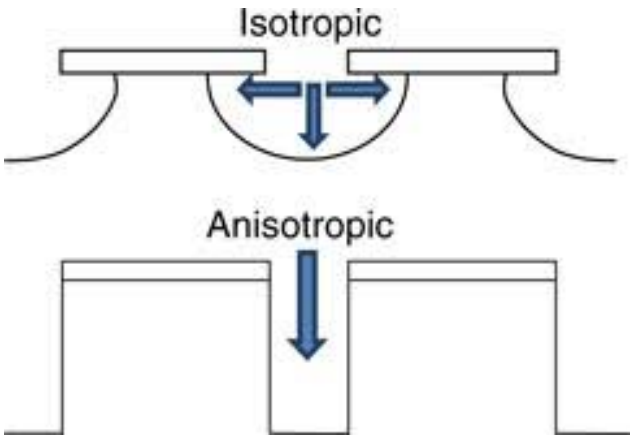

Figure 15: Cross-section diagram showing difference between isotropic and anisotropic etch profiles [30].

Wet etching is a chemical process in which the material is exposed to a liquid that reacts with different rates for the various layers of a device. For example, HF reacts with the silicon dioxide layers at a much greater etch rate than it reacts with the polysilicon layers. The main advantage of wet etching is that it is highly selective. The drawbacks of most wet etching techniques is that it involves submersing in fluid which can be damaging to components and the etching is often isotropic [23]. One of the most popular types of dry etching is reactive ion etching (RIE). RIE was originally developed to be a highly anisotropic etch process. As shown in Figure 16, it works by exciting a gas to an ion state and then bombarding the wafer sample with those ions. When the ions encounter the sample wafer, they react and etch away the sample material. The ions can be controlled with an electric field allowing the direction to be controlled increasing the anisotropy of the etch [23].

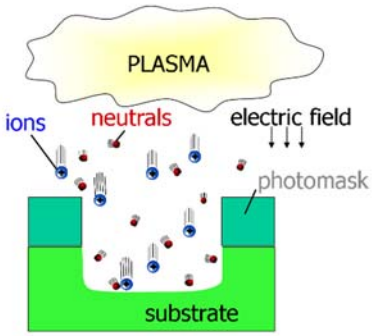

Figure 16: Diagram showing etching using RIE. Ions from the plasma are accelerated by the electric field. When the ions hit the substrate, material is removed [31].

2.3.4 PolyMUMPs

PolyMUMPs is a commercial foundry fabrication process by MEMSCAP. It is a type of Multi-User MEMS Processes or MUMPs and utilizes a standard surface micromachining fabrication process to create three-layer polysilicon devices with a top metal layer. MEMSCAP runs multiple fabrication cycles each year and to have a device fabricated, a user uses a standard L-Edit design template with the different PolyMUMPs layers to design a $1cm^2$ x $1cm^2$ device. MEMSCAP collects all the designs and combines multiple designs into a single mask file to create the required masks to create many devices at once. After all layers have been deposited, the large wafer containing many devices is diced into the individual devices and sent to the customer [18].

Because of the combined fabrication of many devices at once, PolyMUMPs fabrication imposes a significant amount of constraints on what and how a device can be made. A full list of the constraints and more in-depth description of the fabrication process is contained in the PolyMUMPs Design Handbook [18]. The major constraints of the process are that designs are limited to three poly-silicon device layers with a top metal layer, only the top two device layers

are releasable, the individual layer thicknesses and material properties are not changeable, and the design rules specify spacing for different desired features.

PolyMUMPs devices (Figure 17) are built on a 150 mm n-type (100) silicon wafer of 1-2 Ohm-cm resistivity. The surface of the wafer is heavily n-type doped with phosphorus to prevent charge feedthrough. The first layer is a 600 nm thick layer of LPCVD silicon nitride for passivation. The second is a patterned 500 nm thick LPCVD poly-silicon layer (Poly0), followed by a patterned 2.0 µm LPCVD PSG sacrificial layer (1st Oxide). A 750nm dimple layer is patterned and removed from the 1st Oxide layer using RIE. Next, the second polysilicon layer (Poly1) is added and patterned to a thickness of 2.0 µm. Following this a 750nm patterned PSG layer is added (2nd Oxide). The final polysilicon layer is added as a 1.5 µm thick patterned layer (Poly2). The final layer is an evaporated 500 nm thick gold layer (Metal). It is patterned with a process called lift-off and can only be deposited on the Poly2 layer. The Poly1 and Poly2 layers are releasable.

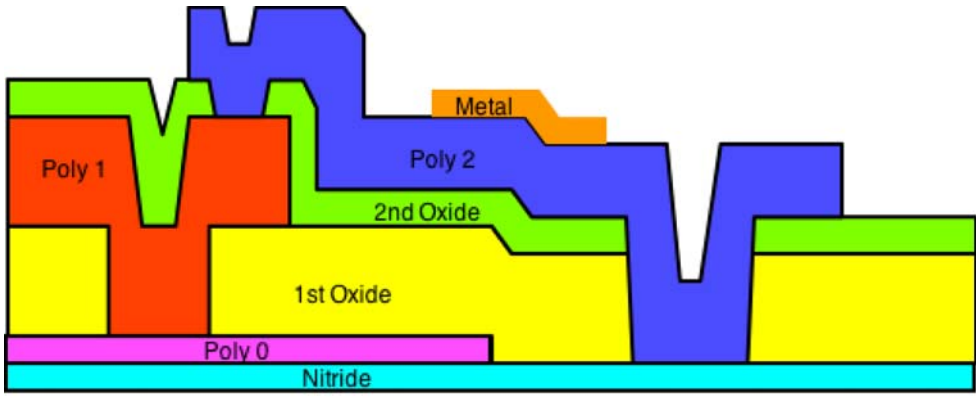

Figure 17: Cross-section of PolyMUMPs process showing available device layers [32]. Note: the dimple etch is not shown.

2.3.5 PolyMUMPs Release

Many MEMS devices must be released either through wet or dry etching in order to be functional. During release (Figure 18) the sacrificial layer of silicon dioxide is removed to allow

portions of the fabricated device to move. PolyMUMPS uses two sacrificial layers of PSG that can be removed using either a wet etch in hydrofluoric acid (HF) or by using a gaseous HF release process. Equation (2) provides the chemical reaction for HF etching silicon dioxide. This reaction can have a selectivity at room temperature of 100:1 [23].

$$SiO_2 + 6HF \rightarrow H_2 + SiF_6 + 2H_2O \tag{2}$$

Figure 18: Diagram showing how sacrificial PSG layers are removed during release etch [18].

2.3.6 Device Bonding and Packaging

For a final device to be useful to an end user, it must be properly packaged. The packaging provides mechanical support and resiliency to damage from environmental and handling damage and allows for a device to be integrated into a larger system. For example, a fabricated MEMS device could be a single chip that is part of a larger circuit board that is itself part of a larger mechanical system such as an automobile. In general, for MEMS there are three levels of packaging: die level, device level, and system (Figure 19) [13]. Die-level packaging as shown in Figure 20 protects the individual chips from damage. Device layer packaging entails protecting the MEMS device as well as the chips and elements that share the same circuit board. Finally, system level packaging requires protecting the full system in use to minimize risk of damage from environmental considerations [33].

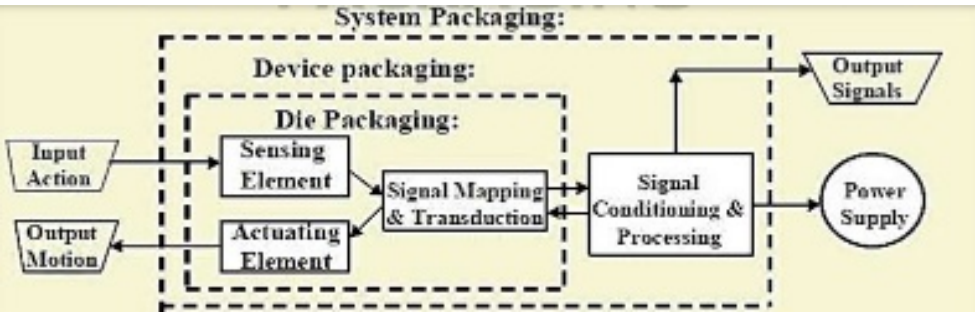

Figure 19: Three levels of microsystem packaging are shown: die, device and system packaging. [22]

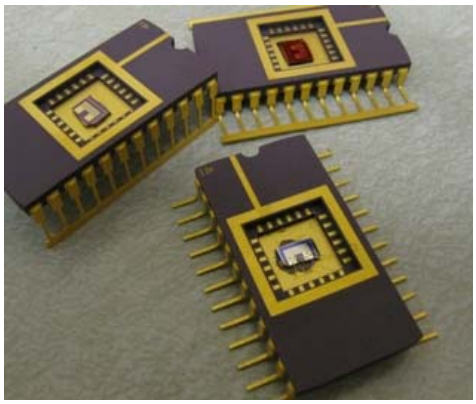

Figure 20: Example of die level packaging for MEMS devices [34].

2.4 Electromechanics

As the name implies, MEMS make use of both mechanical and electrical behaviors of micro-scale materials. Therefore, a knowledge of the underlying electromechanical interactions and principles is important to understand how these devices function and how to design them. The following sections discuss a variety of important electromechanical physical concepts that are of interest to this research area.

2.4.1 Electrostatic Actuation

Electrostatic actuation was first demonstrated in the 1960s by using an AC voltage with a DC bias to move a cantilever beam. Electrostatic actuation is still a very common form of

actuation for MEMS because of the relative ease of fabrication and compatibility with other circuits and devices [1]. The elementary physics principle of electrostatic actuation is that the force causing actuation is from Coulomb's force shown in Equation (3). This equation states that the attractive force is proportional to the magnitude of the two charged particles and inversely proportional to the square of the distance between the two particles.

$$F = \frac{1}{4\pi\epsilon_0}\frac{q_1 q_2}{r^2} \tag{3}$$

To simplify the electrostatic force and associated energy equations, it is common to model the situation as two parallel plates (Figure 21). This simplification is done to find a closed form solution of the simplest case to understand the basic principles. The potential energy of the parallel plates can be expressed as Equation (4) and associated electrostatic force can be expressed as Equation (5).

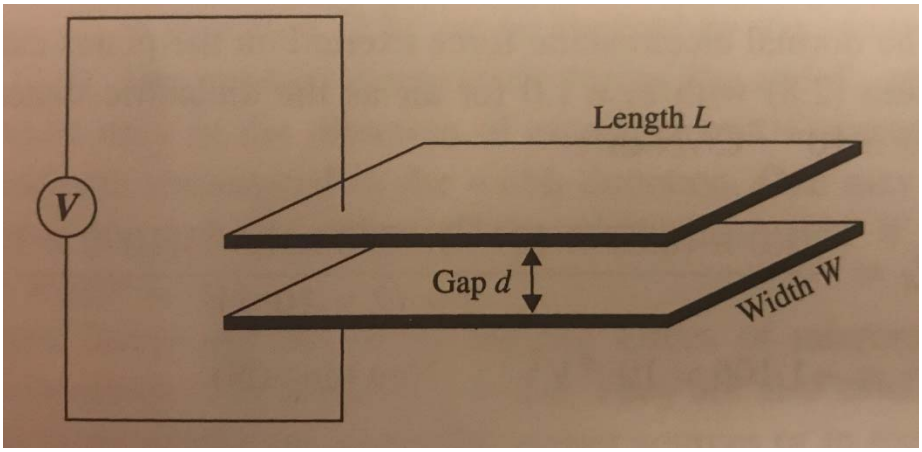

Figure 21: Diagram of parallel plates with a voltage potential of V between them [22]. Used to model potential energy and force.

$$U = -\frac{1}{2}CV^2 = -\frac{\epsilon_r\epsilon_0 WLV^2}{2d} \tag{4}$$

$$F = -\frac{\delta U}{\delta d} = -\frac{1}{2}\frac{\epsilon_r \epsilon_0 W L V^2}{d^2} \tag{5}$$

Equation (5) provides a simple design equation to understand the basic design parameters that can be tweaked in the design process. They include the cross-sectional area of the plate or beam($W * L$), the applied potential (V), the dielectric constant (ϵ_r), and the distance between the plates(d) [22].

2.4.2 Residual Stress and Bimorph Beams

A second type of actuation is thermal actuation. Thermal actuation is caused by the expansion or contraction of material as it changes temperatures. The expansion or contraction is given by δ and is directly related to the Temperature (T) and the linear coefficient of thermal expansion (α). When two materials are layered on top of each other with different coefficients of thermal expansion, this causes different expansion and contraction rates as the temperature is varied. This results in surface strains (ϵ) at the interface of the materials and curvature of the beam as shown in Equation (6)[1]. This is often referred to as a bimorph beam. The change in temperature required for actuation can be caused by Joule heating or by a change in temperature that results after a manufacturing process [22]. Actuation that occurs because of returning to room temperature after a manufacturing process is often called residual stress. Using the surface strain, the radius of curvature for a bimorph beam with differing thicknesses (t_1, t_2), and moduli (E_1, E_2) is given in Equation (7)[35].

$$\epsilon = \frac{\delta_2 - \delta_1}{l} = (\alpha_2 - \alpha_1)(T_b - T_a) \tag{6}$$

$$\frac{1}{r} = \frac{6t(\alpha_2 - \alpha_1)(T_b - T_a)}{4t_1^2 + 4t_2^2 + 6t_1t_2 + \frac{E_1t_1^3}{E_2t_2} + \frac{E_2t_2^3}{E_1t_1}} \quad (7)$$

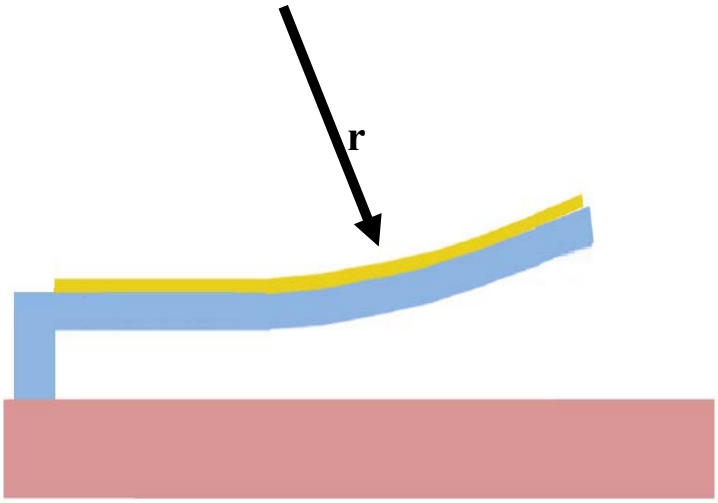

Figure 22: Bimorph beam showing displacement with radius of curvature of r. The top gold layer expands and contracts at a different rate when the temperature changes.

2.4.3 Electrothermal Actuation

Electrothermal actuation is an actuation method that uses Joule heating to create a differential thermal expansion between a 'hot arm' and a 'cold arm'[1] (Figure 23). Joule heating is the heating that occurs in materials as an electric current is passed through them [36]. As shown in the previous section on bimorph beams, a change in temperature will cause a contraction or expansion based on the coefficient of thermal expansion. As shown in Equation (8), the amount of heating (Q) increases with the square of the electric current density (j). The current density is dependent on the total electric current of the circuit (I) and the cross-sectional area (A), so in a circuit, the localized amount of Joule heating will be determined by the cross-sectional area of the circuit element[37]. By varying the cross-sectional area, a 'hot arm' and 'cold arm' can be created. The hot arm will expand more than cold arm creating the actuation.

$$Q = \frac{1}{\sigma}j^2 = \frac{1}{\sigma} * \left(\frac{I}{A}\right)^2 \quad (8)$$

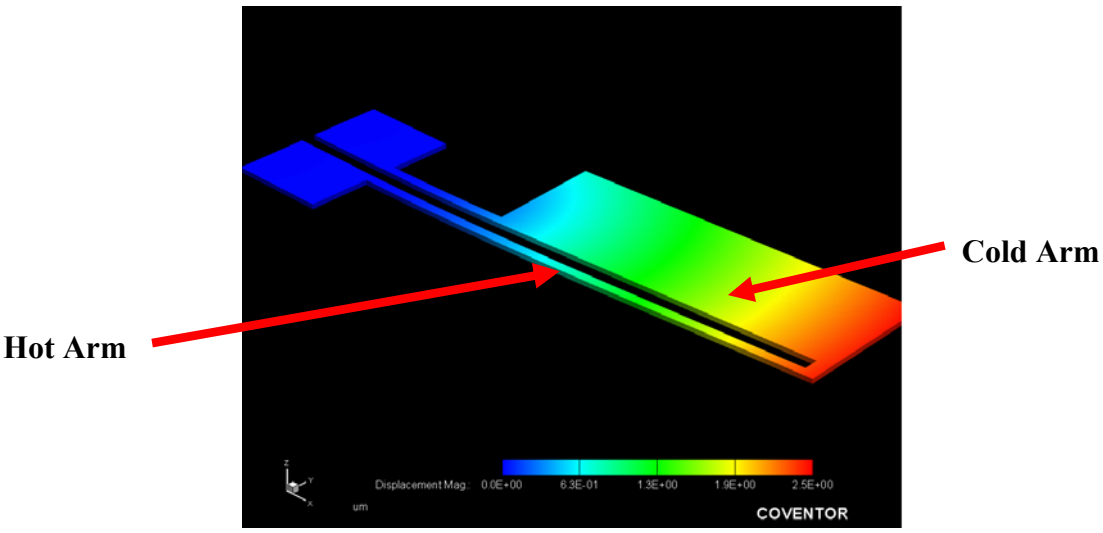

Figure 23: FEA diagram of a simple electrostatic actuation showing the larger relative expansion of the 'hot arm' vs the 'cold arm'. When a current passes through, the hot arm expands more than the cold arm.

2.4.4 Doping Effects on Dielectric Constant

In a semiconductor, doping is used to inject charge carriers either electrons (n-type or holes (p-type) into the crystal lattice [16]. The presence of dopants can change a number of electronic qualities of the semiconductor material including its dielectric constant. For silicon in particular, the addition of donor atoms (N_D) will increase the dielectric constant from its undoped value. Equation (9) provides a relationship for n-type doping of silicon at room temperature using phosphorous [38]. Additional information on doping is provided in Appendix B.

$$\epsilon_r(N_D) = 11.688 + 1.635 * \frac{10^{-19} N_D}{1 + 1.172 * 10^{-21} N_D} \tag{9}$$

2.5 Beam Theory

To understand the mechanical behavior of the MEMS especially as it relates to the cantilever and serpentine beams mechanics, the fundamentals of static and dynamic beam theory

is relevant. This section discusses concepts critical to the discussion of the function and understanding of MEMS.

2.5.1 Euler-Bernoulli Beam Theory

The governing equation to solve beam problem in MEMS is the Euler-Bernoulli beam equation. Equation (10) provides the Euler-Bernoulli equation for the one dimensional case [1].

$$EI\frac{d^4y}{dx^4} = q \tag{10}$$

The Euler-Bernoulli equation can be expanded from the static case to incorporate dynamic time effects. This is commonly referred to as the Euler-Lagrange Equation and is shown in Equation (11).

$$EI\frac{d^4y}{dx^4} + \mu\frac{d^2y}{dt^2} = q \tag{11}$$

While both equations appear straight-forward and are applicable to a wide variety of situations, solving Equation (10) and (11) into a closed form solution for a specific case can be extremely complicated. Each specific case will have a particular geometry, boundary, and loading conditions.

2.5.2 Spring Theory and Young's Modulus

Hooke's Law shown in Equation (13) describes a linear force-displace relationship in simple springs. The concept is also used to describe and characterize the stiffness of structures as shown in subsequent sections [1]. Hooke's law is only applicable if the material is being used in the linear and elastic region. In this region, a material will return to its original state when an applied force is removed. A material property called the Young's modulus (E) as defined in Equation (12) is a measurement of the stress-strain relationship in the elastic region as

shown in Figure 24. If a material is in the non-elastic region, then permanent deformation will remain even after an applied force is removed [39].

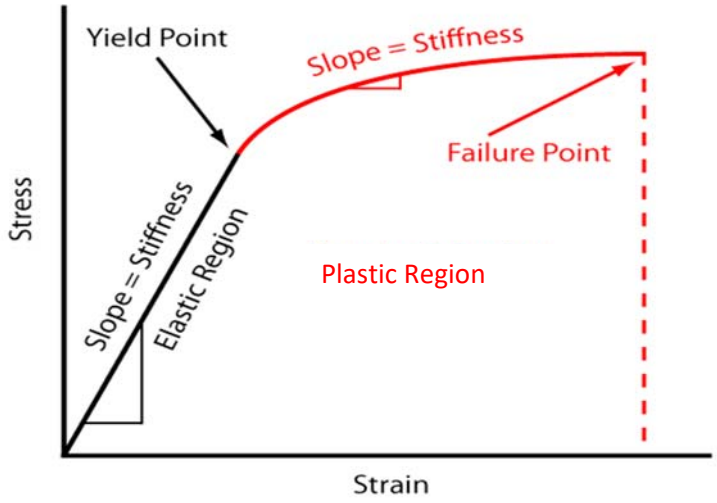

Figure 24: Stress and strain plot for an example showing elastic and nonelastic (plastic) regions [40].

$$E = \frac{\sigma}{\epsilon} \tag{12}$$

$$F = -k\delta = -EA\left(\frac{\Delta L}{L_0}\right) \tag{13}$$

2.5.3 Resonance and Modal Harmonics

Mechanical resonance in a structure is the frequency at which a non-rigid structure will naturally vibrate when perturbed with an excitation force. Many simple MEMS structures can be modeled as a single degree of freedom damped oscillator with a spring restoring force for single mode analysis [41]. Figure 25 shows a depiction of a model for a single degree of freedom damped oscillator. The major components are a mass (m), spring constant (k) based on the structure stiffness, time dependent driving force (u(t)), and dampening constant (c). The differential equation describing the behavior of this system is given in equation (14) . The natural frequency (f) for the system is described as equation (15) [42].

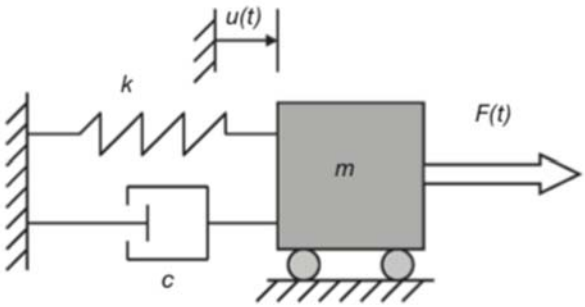

Figure 25: Diagram for a simple single degree of freedom damped oscillator with mass m and spring constant k [41].

$$m\ddot{u}(t) + c\dot{u}(t) + ku(t) = F(t) \tag{14}$$

$$f_0 = \frac{1}{2\pi}\sqrt{\frac{k}{m}} \tag{15}$$

MEMS structures will also display modal harmonics. Modal harmonics is when a structure does not vibrate at a single frequency but can be excited at different modes based on the shape of the excitation. Modal harmonics are highly dependent on the structure shape and boundary conditions and are therefore difficult to solve analytically [41]. One closed form solution is for the free response of a micro-cantilever (similar to the cantilever shown in Figure 28). The free response natural frequency (ω_n) and corresponding mode shape or eigenshape ($\phi_n(\zeta)$) is dependent on differential equation and boundary conditions for a cantilever provided in Equation (15).

$$\phi_n''''(\zeta) - \lambda^4\phi_n(\zeta) = 0, \quad \phi_n(0) = \phi_n'(0) = \phi''(1) = \phi'''(1) = 0 \tag{16}$$

In the above equation, λ_n is the associate mode eigenvalue and relates to the associated natural frequency. ζ is the dimensionless lateral location on the cantilever as shown in equation

(17). Solving for the differential equation provides the mode shape for the first three modes shown in Figure 26[41].

$$\zeta = \left(\frac{x}{L_0}\right) \tag{17}$$

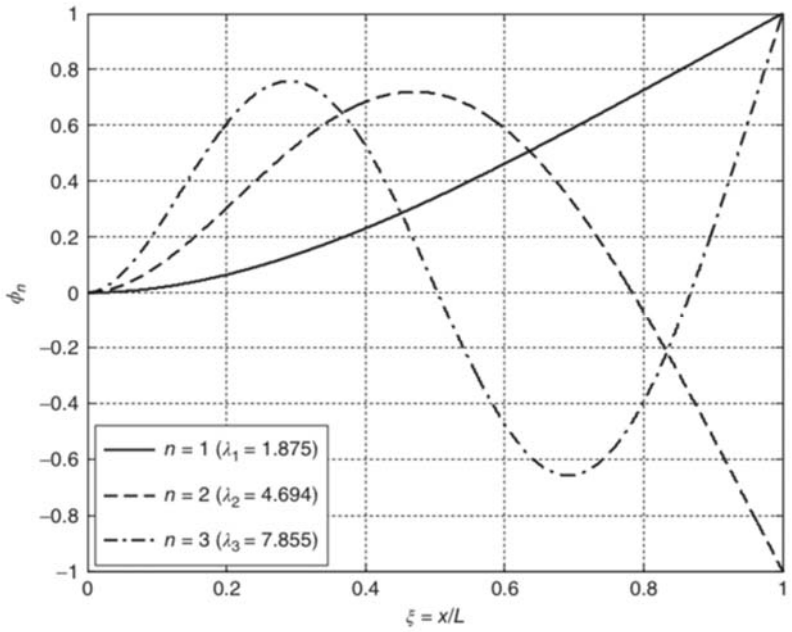

Figure 26: Plot showing first three harmonic mode displacements for the free vibration of a cantilever beam using the eigenshape [41]

2.5.4 Pull-In

Electrostatic actuators using cantilevers like what is shown in Figure 28, demonstrate a phenomenon called pull-in. Pull-in is a saddle-node bifurcation that results in instability and occurs when the electrostatic attractive force from Coulomb's law as shown in Equation (3) increasing at a greater rate than the Hooke's law force shown in Equation (13) [43]. For a cantilever, as the voltage between the beam and the electrode increases, the beam will begin to bend toward the electrode. However, once a voltage above the pull-in voltage is reached, the beam will then suddenly snap into place. Pull-in limits the usability of electrostatic actuators because it severely reduces the stable displacement solutions for a given configuration (Figure

27)[44]. In addition to reducing the available deflection angles, the dynamics of pull-in can cause failures in the MEMS structure. Failures can be caused by sudden electrical discharge/static discharge between the beam and electrode, dielectric charging, or stiction[43].

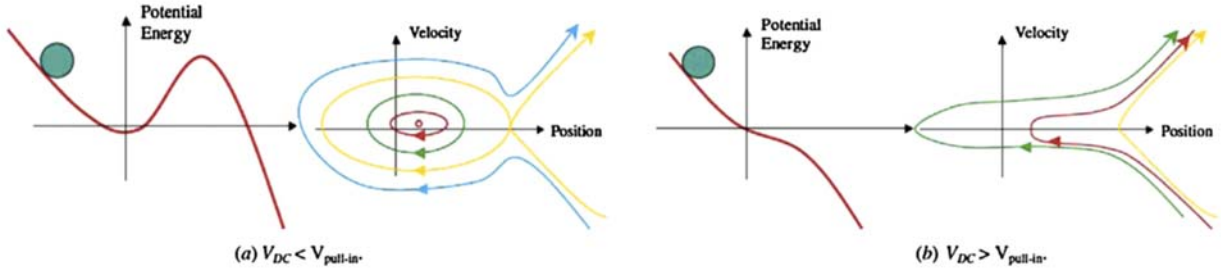

Figure 27: (a) shows the potential energy diagram and phase portrait when in a stable configuration at a voltage under pull-in and (b) shows the potential energy and phase portrait at an unstable voltage greater than the pull-in voltage [43].

2.5.5 Electrostatic Cantilever Beam

To solve for the case of a cantilever beam actuator (Figure 28) that is actuated by electrostatic force across the length of the beam, the boundary conditions are at $x = 0$: $y = 0$ and $\frac{dy}{dx} = 0$ and at $x = l$: $\frac{d^2y}{dx^2} = 0$ and $\frac{d^3y}{dx^3} = 0$. The force is similar to that which was found in Equation (18) [1].

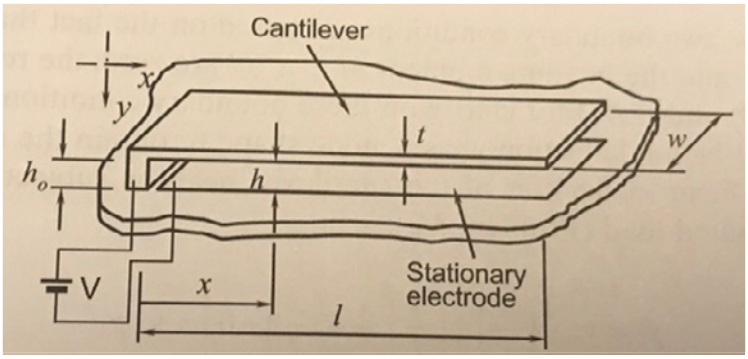

Figure 28: Diagram of electrostatically actuated cantilever beam used for derivation pull in voltage [1].

$$EI\frac{d^4y}{dx^4} = \frac{1}{2}\frac{\epsilon_r\epsilon_0 wV^2}{(h_0 - y)^2} \tag{18}$$

Solving for the spring stiffness (k) results in Equation (19).

$$k = \frac{16}{5}\frac{EI}{l^3} \tag{19}$$

By balancing the spring force with the electrostatic force the pull-in voltage is found in Equation (20)[1].

$$V_{pi} = 0.5297\sqrt{\frac{Et^3h_0^3}{\epsilon_r\epsilon_0 l^4}} \tag{20}$$

2.6 FEA Modeling

Closed form solutions of the Euler-Bernoulli equation for complicated design geometries are extremely difficult to derive. The previous section describing modal harmonics and pull-in get complicated even just for a simple cantilever beam. Because of this, finite element analysis (FEA) and modeling is used. FEA is usually accomplished using a computer program such as Coventorware or ANSYS [39][45]. FEA is accomplished through discretization. Each surface or volume of structure is divided into a finite number of elements connected at nodes. This can cause a loss of fidelity depending on the size of elements and number of nodes. After the discretization, known load conditions $\{Q\}$ such as heat, rigid boundaries, and voltage are applied to the model. The shape of the geometry effects the element coefficient matrix $[K]$ and the computer solves Equation (21) to find the unknown quantity at the nodes $\{q\}$[22]. This equation looks simple, but FEA models get larger and more complex, it creates larger and larger coefficient matrices to solve resulting in large computational demand.

$$[K]\{q\} = \{Q\} \tag{21}$$

In practical terms, FEA allows designers to build a computer model of a design and simulate how that design will perform based on various inputs to a much higher fidelity than

calculating by hand allows. Both Coventorware and ANSYS provide a multiphysics platform that allow for the calculation of various quantities for MEMS designs such as electrostatics, electrothermomechanics, harmonics, and transient behavior. One way to control the computational requirements for solving is to change the mesh. The mesh determines the location and number of nodes. Increasing the mesh density can increase accuracy, but it will reduce computational efficiency [46].

2.7 Previous Work

This research is focused on developing segmented control for an electrostatically actuated high-displacement micro-mirror for use in a future micro-mirror array. There is several previous technologies and research efforts that this current research builds off. The first large scale commercial application of micro-mirror arrays was by the Texas Instrument corporation and their DMD technology. It uses up to two million individual micromirrors for each of its display chips. Each acts as an individual pixel for a display. The DMD uses electrostatic actuation and has shown fast actuation and high reliability for mirror actuation with reliability demonstrated at 5.30×10^{12} cycles for each mirror in an array and actuation rates shown at 16 milliseconds [47]. The DMD demonstrated the feasibility of a similar technology to what is proposed in this research, the major limitation of the DMD was that it had a small actuation angle of +/-12° and did not have any intermediate step locations, the pixels were either on or off.

Research has previously shown the ability to control a single electrostatically actuated beam piecewise with unique electrode shapes [48]. In their research, they demonstrated that with a single electrode that has unique geometries allows for multiple stable pull-in configurations. They did not show their design with a serpentine cantilever and did not attempt multiple electrodes.

For the design that is used in this research effort, its effectiveness was first demonstrated by Walton and Starman [49]–[51]. They demonstrated the effectiveness of using the serpentine bimorph design for a high-angle mirror deflection. They have demonstrated significant improvement in increasing the deflection angle from other similar beam steering arrays using similar geometries [52], [53] by the use of bimorph serpentine beams. Further improvements to increase the maximum deflection of the bimorph design from 50 microns to 400 μm has been recently demonstrated by applying a high-stressed (-2GPa) nitride layer with an opposite residual stress of the metal compression force. This was demonstrated to force an inflection point in the bimorph beam, greatly increasing the initial deflection [51].

3. Methodology

The following sections provide a description of the methodology used to come up with the design, modeling, and testing of the devices. The concept of the devices is based on micro-mirror actuator arrays previously built and tested by AFRL and AFIT researchers. The design uses bimorph serpentine beams located around a base to provide a platform for electrostatically driven large deflections [49], [50], [51]. The final desired design will include an array of the bimorph serpentine beam platform with post and mirrors attached for beam-steering (Figure 30).

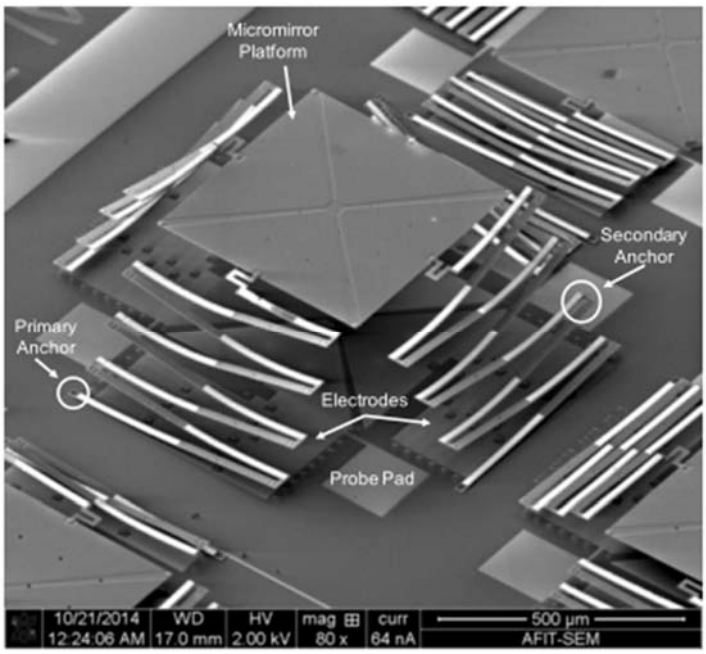

Figure 29: SEM of previously tested AFRL and AFIT devices [50].

This novel device has shown quite a promise for large angular deflections. One major limiter to the design was that a method of controlling the angular platform over a wide margin of displacement angle had not yet been demonstrated. This work investigates a method that could be used independently or together to control the micro-mirrors using segmented channels.

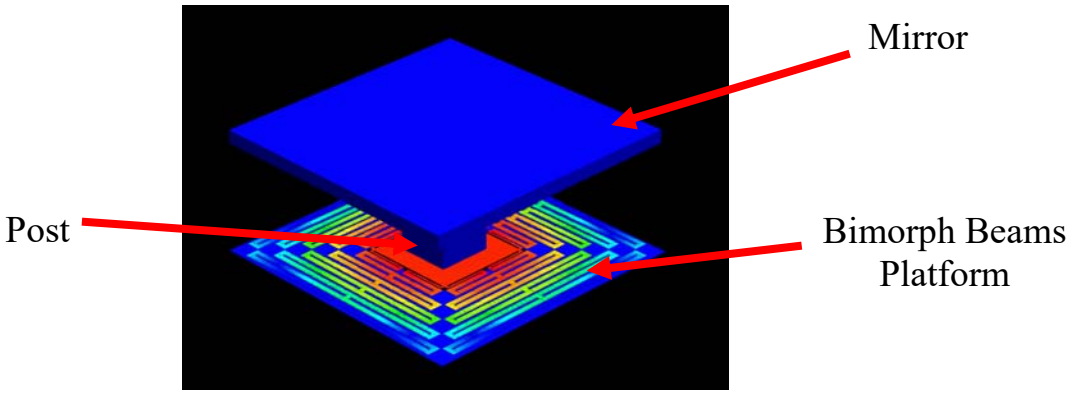

Figure 30: 3D model of 10-beam electrostatically actuated mirror, post and bimorph beam platform. This is a rendering of a single mirror for the proposed prototype high-angle beam-steering micromirror array.

3.1 Design

The segmented electrode design consists of multiple individual electrodes that are geometrically designed to be electrically isolated from the actuating beam instead of a single actuation electrode that can come into contact of the beam. The segmented electrodes are intended to allow for improved control with the actuation of the device. Two approaches were taken to electrically isolate the electrodes from the serpentine beam structure: electrode covers and electrode posts. Additionally, there are two ways in which the device was operated and tested in: electrostatic and capacitive sensing mode. A further explanation of what is meant for each of these modes is provided in future sections. Figure 31 provides a top view of the segmented electrodes and how the segmented electrodes are integrated with the full mirror structure and Figure 32 provides an SEM of one of the fabricated devices.

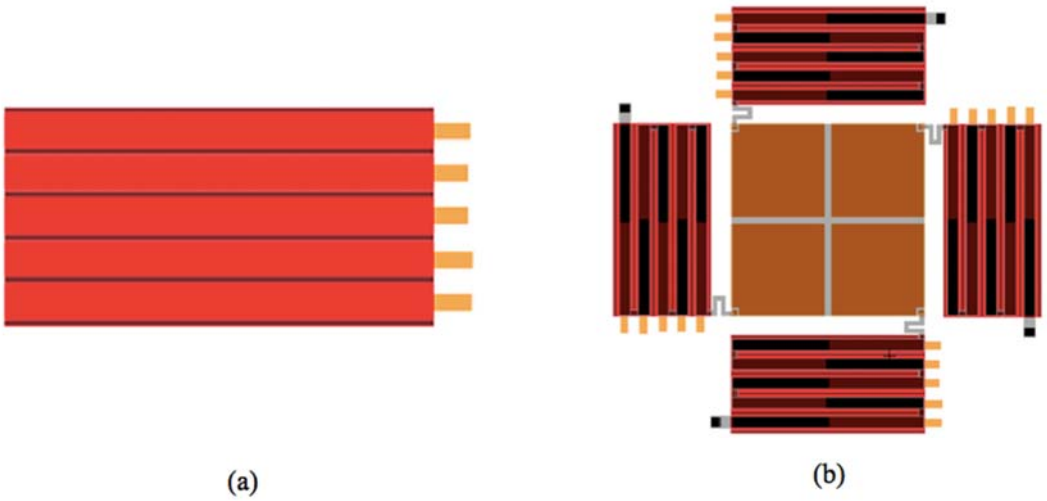

(a) (b)

Figure 31: MEMS structural concept of the covered segmented channels with individual electrodes. (a) illustrates a five-channel segmented channel individual electrode design. (b) illustrates the design integrated underneath a five-arm serpentine bimorph mirror.

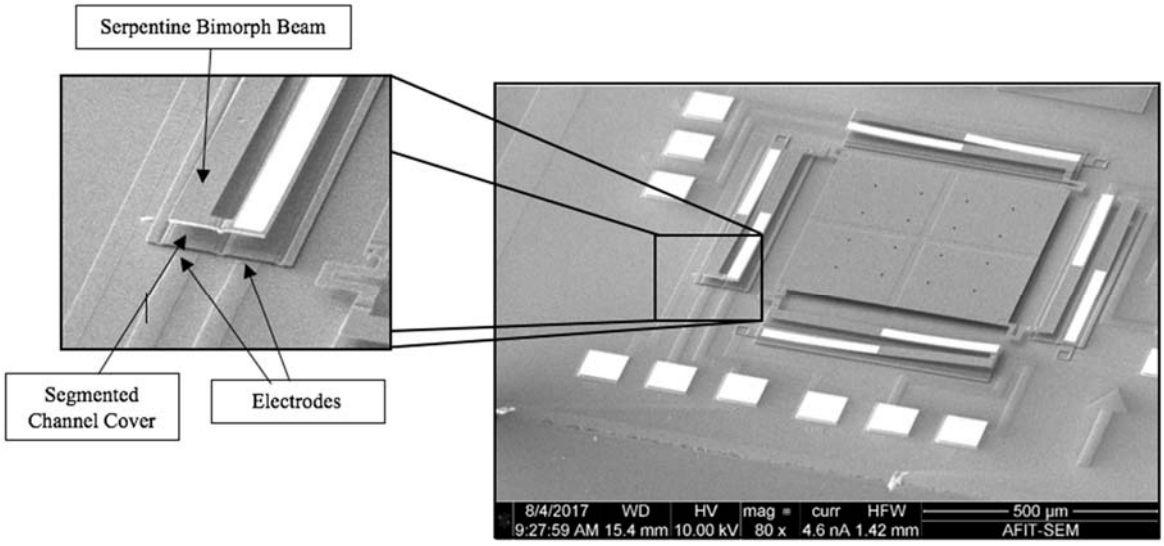

(a) (b)

Figure 32: An SEM image of a two-channel electrode cover fabricated device. (a) depicts the entire device with the invention integrated underneath a two-arm serpentine bimorph

beam. (b) depicts an enlargement of a portion of the invention depicting the segmented changes and electrodes.

3.1.1 Electrode Cover Design

The first design to be built and tested was the covered electrode design. It consists of the individual electrodes that are created out of the PolyMUMPs Poly0 layer. To isolate the electrodes from contact with the serpentine beam structure, they are covered by the Poly1 layer. The serpentine beam consists of the Poly2 and metal layers (Figure 32).

3.1.2 Electrode Post Design

The second design style consists of using electrically isolated posts throughout the electrode and have them protrude up (Figure 33). In this design, the individual electrodes are patterned out of the Poly0 layer, however, small rectangles are cut out of the electrodes and Poly1 posts protrude out of the holes. The Poly1 posts are anchored to the nitride layer. The purpose of these posts is to contact the serpentine beam as it actuates to keep the beam from contacting the actual electrodes. The electrode cover design was modified to this because of concerns of using the Poly1 layer as the separation layer between the serpentine beam. This is because the Poly1 layer is a doped polysilicon layer and could potentially behave like a conductor in ways that are not desirable.

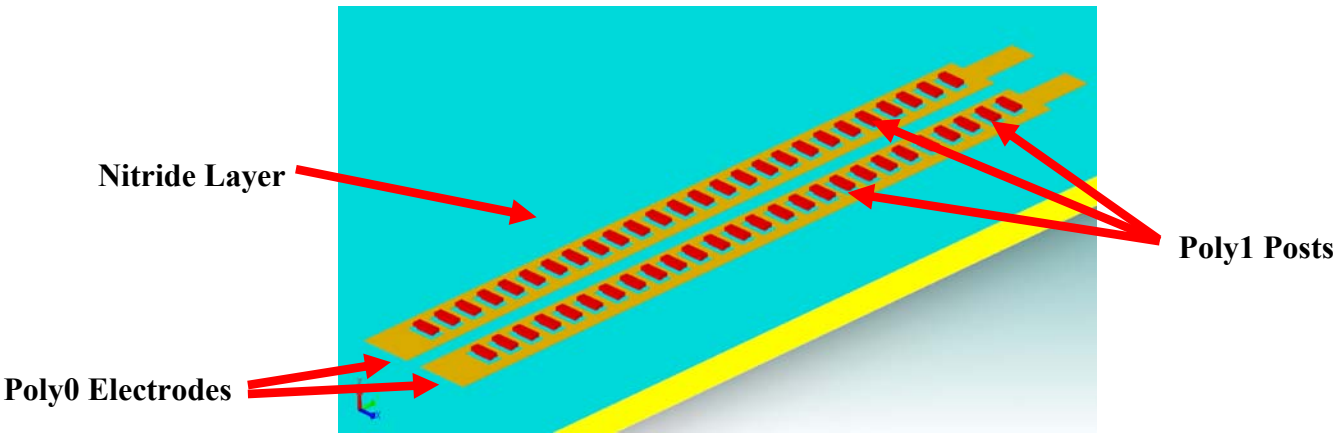

Figure 33: 3D Rendering of a two-channel electrode post design.

3.1.3 Operation in Electrostatic Actuation Mode

The first mode of operation is that a voltage can be applied to individual electrodes causing portions of a serpentine beam to actuate. To operate in this mode, a voltage difference must be applied to one or multiple electrodes and the beam that is sufficient to cause enough electrostatic force to cause actuation. Multiple configurations were tested and was not limited to two electrodes as shown in Figure 32. Five-segment designs were also fabricated as shown in Figure 34.

3.1.4 Operation in Capacitive Sensing Mode

The second operational mode of the device is the capacitive sensing mode. To operate in this mode, the beam must be actuated with an actuation method such as electrostatic or electrothermal actuation. The bending of the beam causes a measurable change in capacitance between the beam and each individual electrode. This difference can be measured and could be used to create a closed loop control system.

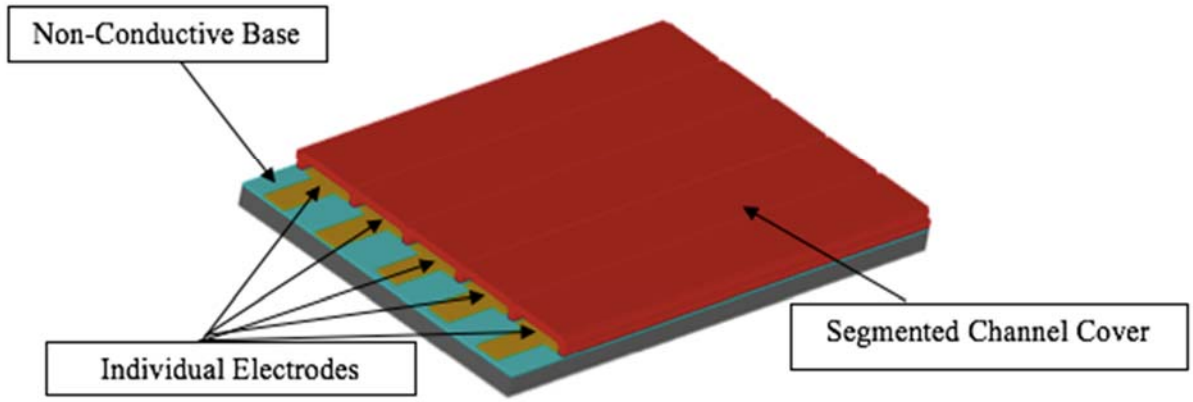

Figure 34: 3D cross-section of the individual electrodes encased in segmented channels for a five-channel design

3.1.5 Electrostatic vs Electrothermal actuation

This research effort focuses on segmented control using electrostatic actuation. However, electrothermal actuation is a valid way of actuation for this of bimorph serpentine beam type of structure [51]. Advantages of electrostatic actuation are faster actuation rates and less possibility of thermal creep as compared to electrothermal actuation[6]. Disadvantages of electrostatic actuation are pull-in instability effects and higher actuated voltage requirements[36]. These designs for testing focus on a design that can be electrostatically actuated. Another method of actuating these devices could be through electrothermal actuation. The possible future advantage of the segmented control design would be when in capacitive sensing mode. That future design could use electrothermal actuation while using the segmented channels as capacitive sensing electrodes to determine position for a feedback controller.

3.2 Modeling

To predict the performance of the designs and to better understand the behavior of the devices, modeling was used before the fabrication of the devices. On the basic level, design

equations such as those listed in Chapter 2 provided a foundational understanding of what were the key variable that should guide the design to get a desired performance. Next, FEA modeling was used as a way for a proof of concept or to ensure that what the device design was based on sound physics principles. Next, FEA analysis was used to give an approximation of what values could be expected from the device during actual testing and characterization. Following this approach, initial models were simple and had minimal design details, however with progressive iterations, model increased in detail and size to increase the fidelity of the results but also requiring much longer computation time. Figure 35 shows an early FEA analysis used to demonstrate the proof of concept that by adding a voltage to a single electrode, displacement of the beam could be controlled.

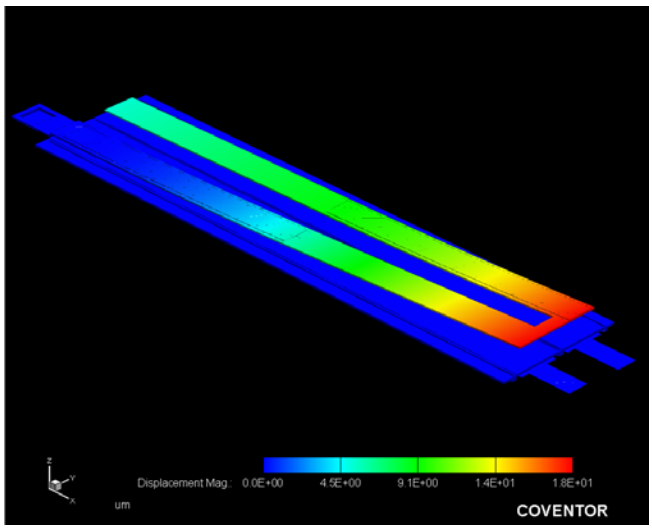

Figure 35: FEA modeling of electrostatic actuation of a two-arm serpentine bimorph beam by an individual electrode on a two-channel design. For the model a voltage of 25V was applied to electrode 2 while no voltage was applied to electrode 1.

3.3 Device Fabrication

After design and modeling, the devices were fabricated to provide a prototype for testing and characterization. Both commercial and in-house processing was used to create the device. The following sections provide further details with regards to device fabrication.

3.3.1 PolyMUMPs

The PolyMUMPs foundry process by MEMSCAP as detailed in Chapter 2 was used for the majority of the fabrication. PolyMUMPs was chosen because of its fast turnaround for manufacturing and it provided an adequate process with enough layers for the fabrication of a prototype. As shown in Figure 36 and Figure 37, two PolyMUMPs designs were submitted the first was for run #119 and the second was for run #121.

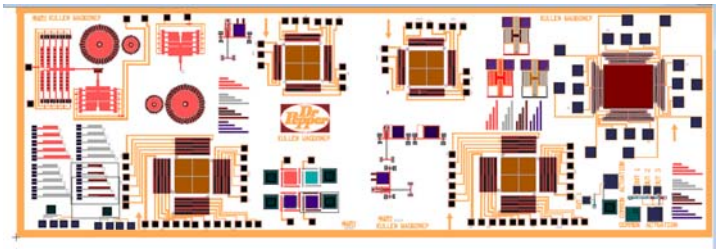

Figure 36: Image of PolyMUMPs L-Edit design for run #119. For this run, only .33 cm^2 was available for use. This design include 2 two-beam covered electrode designs, 2 four-beam covered electrode designs, and 1 six-beam covered elecrode design.

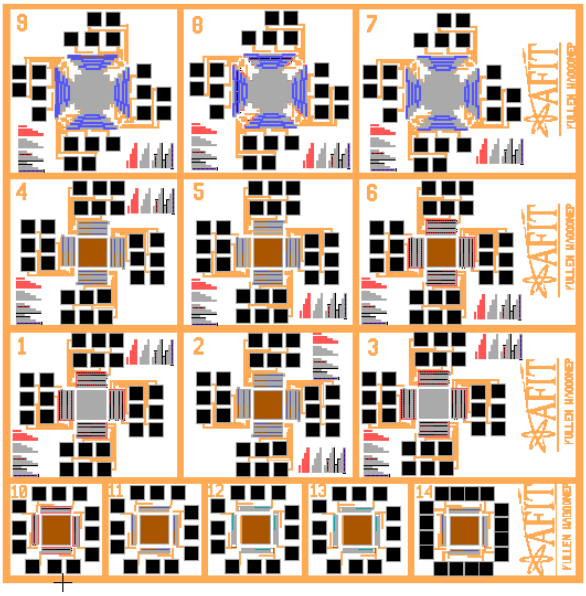

Figure 37: Image of PolyMUMPS L-Edit design for run #121. It included two-beam, four-beam, and ten-beam covered electrode and electrode post designs.

3.3.2 Post Fabrication Processing

After the completion of the PolyMUMPs, the devices were received unreleased to the AFIT cleanroom. Post fabrication processing involved an HF wet etch release with a CO_2 critical point dryer as described to minimize malfunction of devices due to stiction.

3.4 Device Characterization and Testing

Characterization was completed in the AFIT characterization lab. To test the device and measure surface deflection, we used a 3D optical surface profiler, ZYGO® NewView™ 7300 white light interferometer with probe test stations as shown in Figure 38. It allowed us to provide a voltage to the individual electrodes while measuring the deflection of the beam. Figure 39 shows an example readout from the Zygo during testing. The Zygo provided the required measurements of vertical displacement and angular tilt for all three dimensions by providing a topographical measurement of the entire device.

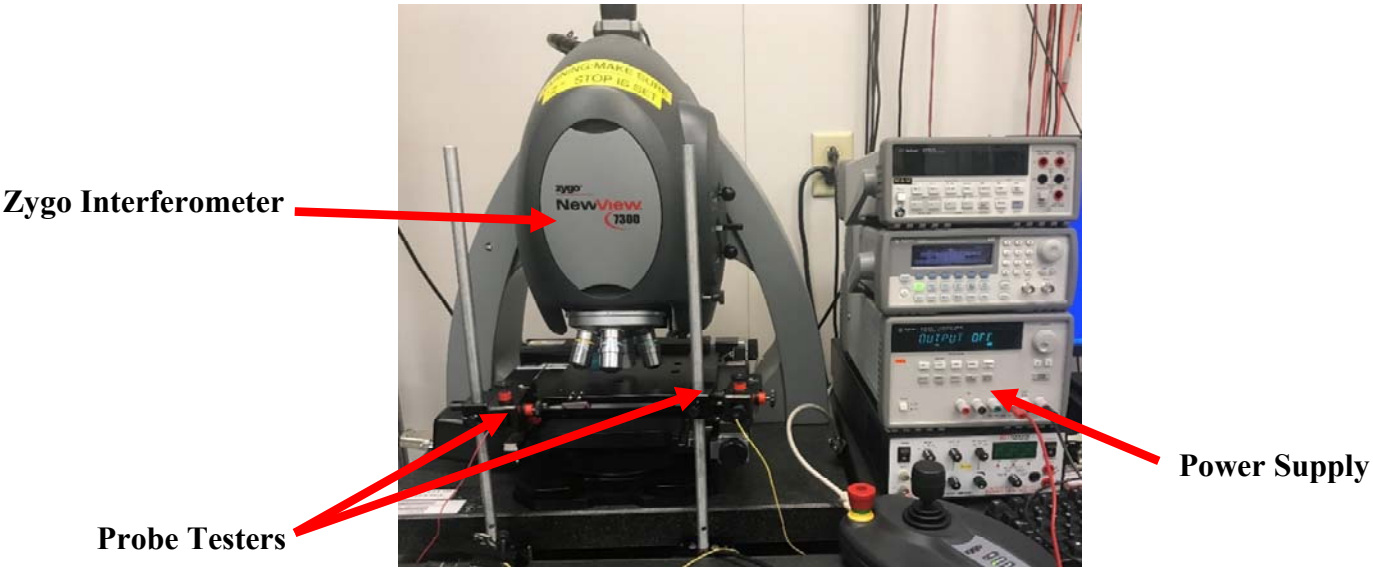

Figure 38: Zygo interferometer with micro-actuating probe testers. The probe testers are used to conduct a voltage from the power supply to the conduct pads.

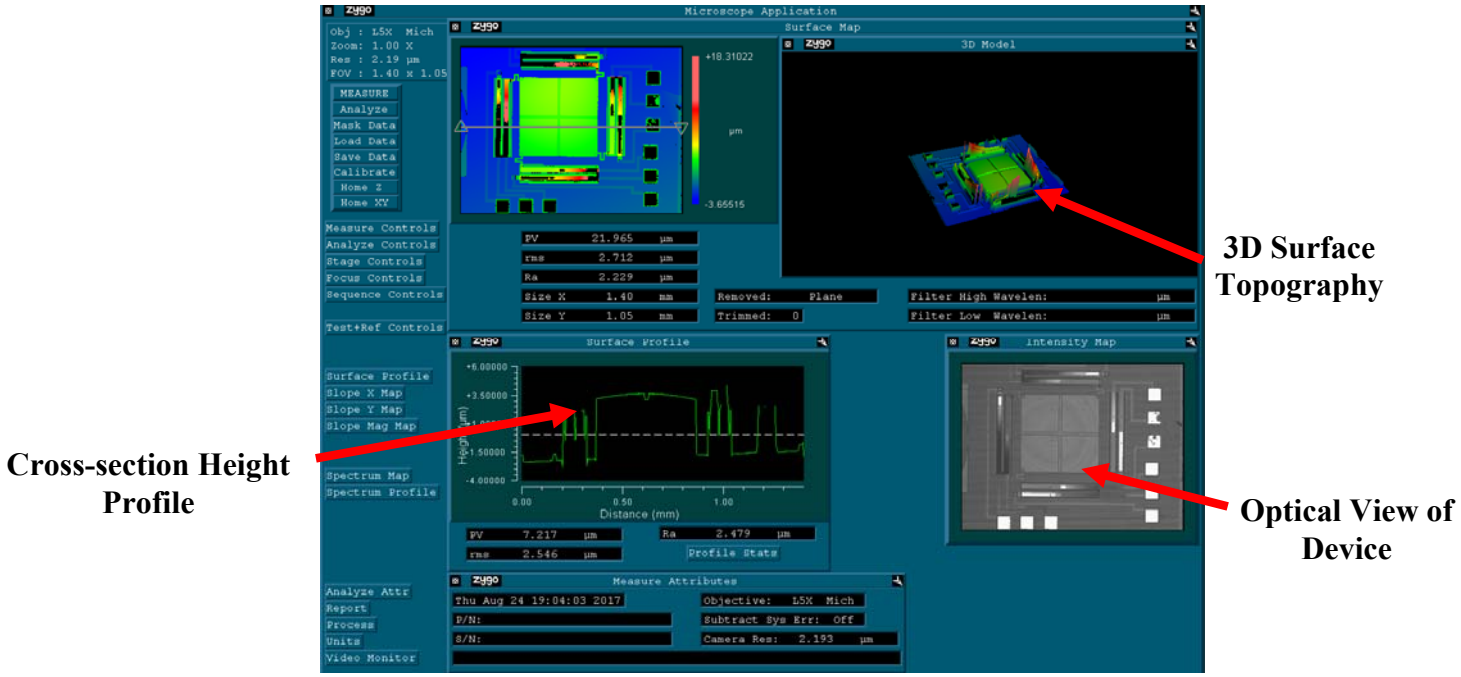

Figure 39: Zygo interferometer readout showing a serpentine beam structure at 0V.

Testing was completed by connecting the micromanipulators from probe station to the positive and negative leads of the DC power source. The micromanipulators were then maneuvered so that they would contact the appropriate and required pads. The power source was then adjusted to the desired voltage for the test point. After application of the voltage, the measurement was made using the Zygo to measure topography, vertical displacement, and angular displacement of the micro-mirror.

3.4.1 Test Variables

For laboratory testing of the structures there were two main control variables: voltage and type of structure and one response variable displacement. The following sections detail the definition of these main control variables.

3.4.1.1 Voltage – Control Variable

This is defined as the voltage of the serpentine beam structure with reference to the electrodes. It is applied by the probe station to the device. A DC power source is used to create the voltage. This is a numerical and continuous with values from 0 to 100V.

3.4.1.1 Type of Structure – Control Variable

This is a categorical variable and there are two characteristics that vary with the structure. The first is the type of structure (post electrode or covered electrode) and number of serpentine segments on each side of the mirror platform (2, 4, or 10).

3.4.1.1 Height Displacement – Response Variable

The height displacement is the measured height of the platform. The platform is actuated using electrostatic force from the electrodes and the height is measured using the interferometer. Height displacement is a numerical and continuous variable.

4. Data

4.1 Chapter Overview

The following sections provide collected data from modeling and testing. Modeling was conducted using simplified closed form solutions and FEA computer simulations. Testing was conducted using released PolyMUMPs devices in the AFIT characterization lab.

4.2 Analytic Modeling Results for two segment section

The following sections detail estimations for calculating various parameters associated with the segmented control of the electrostatically actuated mirror. In order to be able to solve closed forms of the following equations, assumptions and simplifications of the geometries were made. When such assumptions and simplifications were made, they are stated what and why they were chosen.

4.2.1 Estimation of Spring Constant (k)

To estimate the spring constant of a two-segment section, the two segments of the bimorph beam were assumed to be extended to create one long segment as shown in Equation (22). Additionally, to simulate the effects of the other bimorph beams attached to the platform for when only a single beam is actuated, the other bimorph beams were treated as springs in parallel as shown in Equation (23). The curvature of the beam due to the bimorph is not taken into consideration for the calculation of the spring constant. Additional information for calculations is provided in Appendix C.

$$k = \frac{16}{5}\frac{EI}{l^3} = 0.00426\ N/M \tag{22}$$

$$\frac{1}{k_{eff}} = \frac{1}{k_1} + \frac{1}{k_2} + \frac{1}{k_3} + \frac{1}{k_4} = 0.00107 N/m \tag{23}$$

4.2.2 Calculation of pull-in for single section

To estimate the required pull-in voltage for the first two single sections of the bimorph beam when voltage is applied to a single electrode. To calculate this, it is modeled as a single cantilever beam using the closed form solution for a cantilever beam with a single electrode. The midpoint of the curvature is estimated as the constant distance for the electrode to cantilever beam distance for simplification. The height of the midpoint used for the calculation is the height of the midpoint of the two-beam FEA (4.7 μm and 9.4 μm).

$$V_{pi} = 0.5297 \sqrt{\frac{E t^3 h_0^3}{\epsilon_r \epsilon_0 l^4}} = 14.7V, 41.6V \tag{24}$$

4.2.3 Resonant Frequency

To estimate the resonant frequency two methods were used. The first method used was to find an estimation of the first mode resonant frequency f_0 using the simple harmonic oscillator equation and the effective spring constant found in a prior section shown in Equation (25) . The second method employed was to use the estimation of the first three modes as shown in Equations (26)-(29), [41-42].

$$f_0 = \frac{1}{2\pi} \sqrt{\frac{k_{eff}}{m}} = 300\ Hz \tag{25}$$

$$f_n = \frac{\lambda_n^2}{2\pi} \sqrt{\frac{k}{m}}\ for\ \lambda_1 = 1.875, \lambda_2 = 4.694, \lambda_3 = 7.855 \tag{26}$$

$$f_1 = \frac{\lambda_1^2}{2\pi}\sqrt{\frac{k_{eff}}{m}} = 1042\ Hz \tag{27}$$

$$f_2 = \frac{\lambda_2^2}{2\pi}\sqrt{\frac{k_{eff}}{m}} = 6534\ Hz \tag{28}$$

$$f_3 = \frac{\lambda_3^2}{2\pi}\sqrt{\frac{k_{eff}}{m}} = 18296.7\ Hz \tag{29}$$

4.3 Finite Element Modeling Results

The following sections detail FEA results. All analysis was completed using an AFIT MEMS lab workstation with Coventorware software licensed to AFIT. Models were completed using at first simple models followed by more complex models.

4.3.1 Two Segment Mirror Section

FEA was completed on a two-segment mirror section. In this simulation, the platform is not modeled. Pull-in and capacitance analyses were completed and are shown below in Figure 40 and Table 3. This model is expected to give an underestimate of the pull-in voltage because stiffening effects from the other three bimorph beams connected to the central platform are not accounted for when doing the pull-in analysis. Additional analysis was complete (Table 3-Table 5) to determine if capacitive sensing using actuation with one electrode and measuring changes in capacitance with another was feasible.

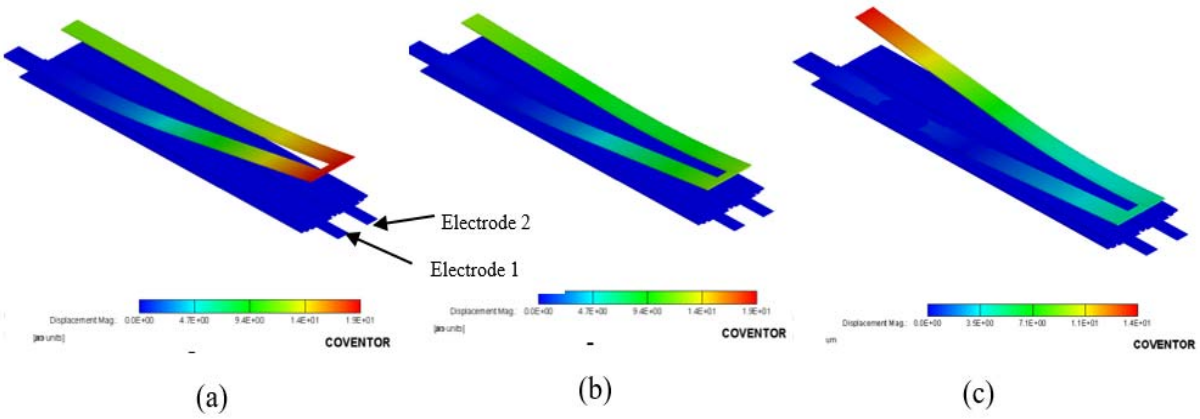

Figure 40: FEA modeling of electrostatic actuation of a two-section bimorph beam by an individual electrode on a two-channel design. For the model a voltage was applied to electrode 1 while no voltage was applied to electrode 2. Figure (a) depicts 0V applied to electrode 1. Figure (b) depicts 18V applied to electrode 1 before pull-in. Figure (c) depicts 24V applied to electrode and shows pull-in of single section of the beam.

Table 3: FEA model results for response of two-beam covered structure when a voltage is applied to electrode #1. This table shows a change in beam vertex height

Electrode #1 Voltage (V)	**Height of Beam Vertex (µm)**
0	18.54
6	18.32
12	17.38
18	11.78
24	4.72

Table 4: FEA analysis data for response of two-beam covered structure when a voltage is applied to electrode #1 and the capacitance between electrode #2 and beam.

Height of Beam Vertex (µm)	**Capacitance Electrode #2 to beam (fF)**
18.98	18.65
18.12	18.79
17.41	19.41
16.72	20.11
16.03	20.90

Table 5: FEA analysis data for response of two-beam covered structure when a voltage is applied to electrode #2 and the capacitance between electrode #1 and beam.

Height of Beam Vertex (µm)	Capacitance Electrode #1 to beam (fF)
19.01	36.22
18.84	36.43
18.36	37.88
18.14	38.32

4.3.2 Two Segment Mirror

FEA analysis as was completed on a full two-segment mirror to determine behavior of the electrostatic actuation and pull-in when pull-in (Figure 43) is conducted on different selections of mirrors. Additional simulation was performed to determine thermomechanical (Figure 41) and harmonic behavior (Figure 42). The thermomechanical analysis was performed to determine the effect of change in temperature on the vertical displacement of the mirror structure.

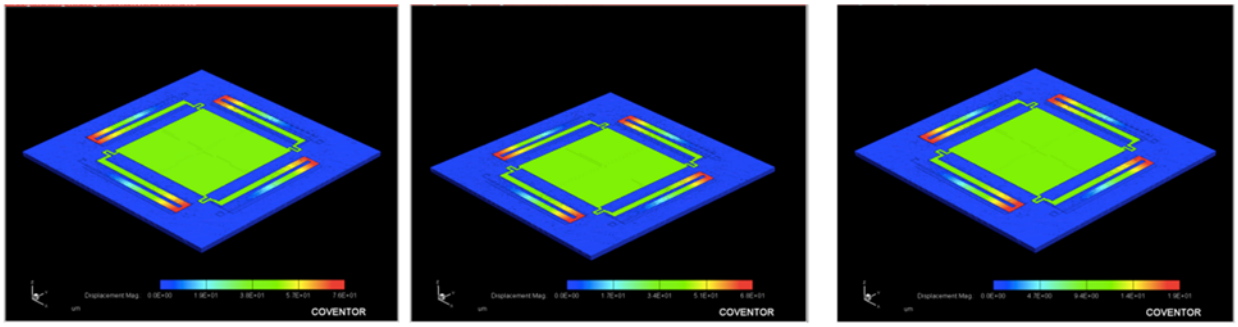

(a) (b) (c)

Figure 41: Thermomechanical FEA results at (a) 100K, (b) 273K, (c) 500K. The maximum amount platform displacement was dependent on the temperature.

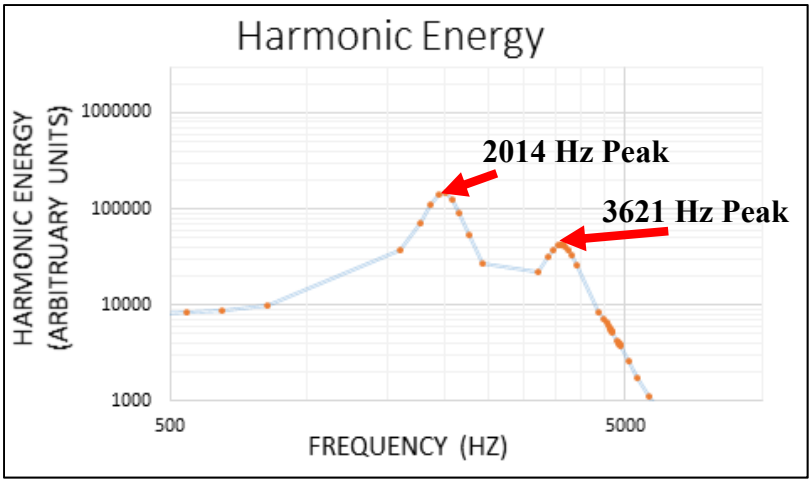

Figure 42: Two-segment mirror harmonic analysis. Plot of FEA data showing two peaks of harmonic energy at 2014 Hz and 3621 Hz.

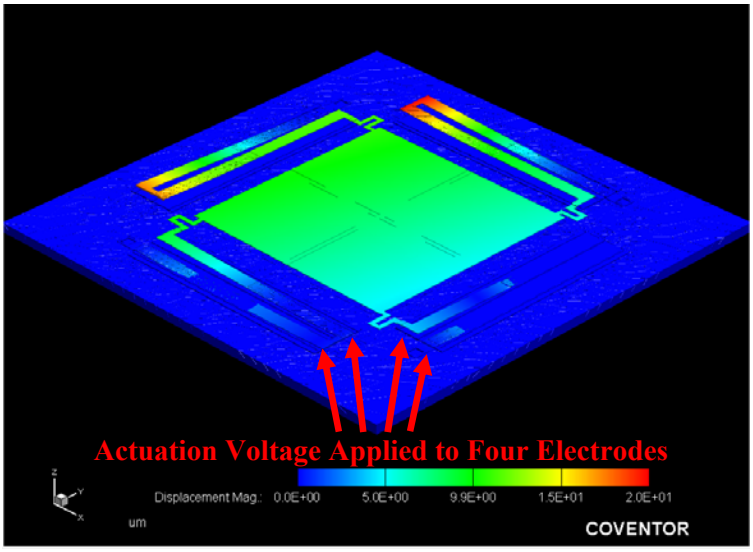

Figure 43: Electrostatic actuation image of two-beam mirror model with pull-in actuation voltage applied to four electrode segments. The mirror deflection is 0.477 degrees.

4.3.3 Two Segment Mirror – Nitride Layer

FEA analysis was completed on a full two-segment mirror to determine behavior of the modal harmonics (Figure 44) and pull-in when a -2GPa layer of nitride is added to increase displacement.

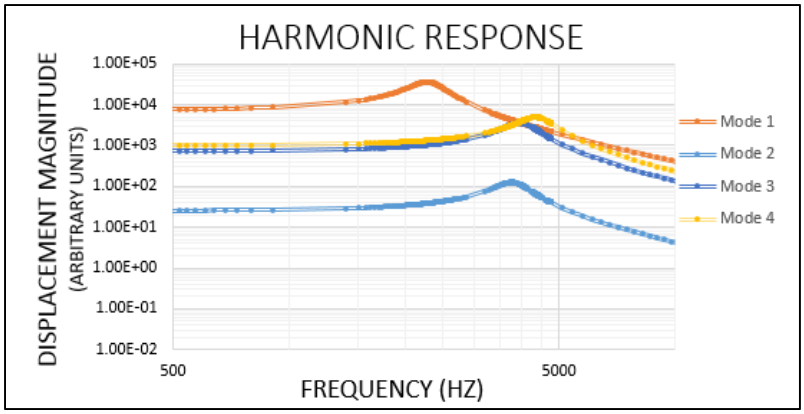

Figure 44: Harmonic response of two-beam mirror with added -2GPa residual stress nitride layer.

4.3.4 Ten Beam No Nitride

The following analysis (Figure 45) is a 300K thermomechanical analysis completed with the AFRL design ten-beam bimorph beam. The -2GPa nitride layer was not added. The maximum displacement was 3.8 µm.

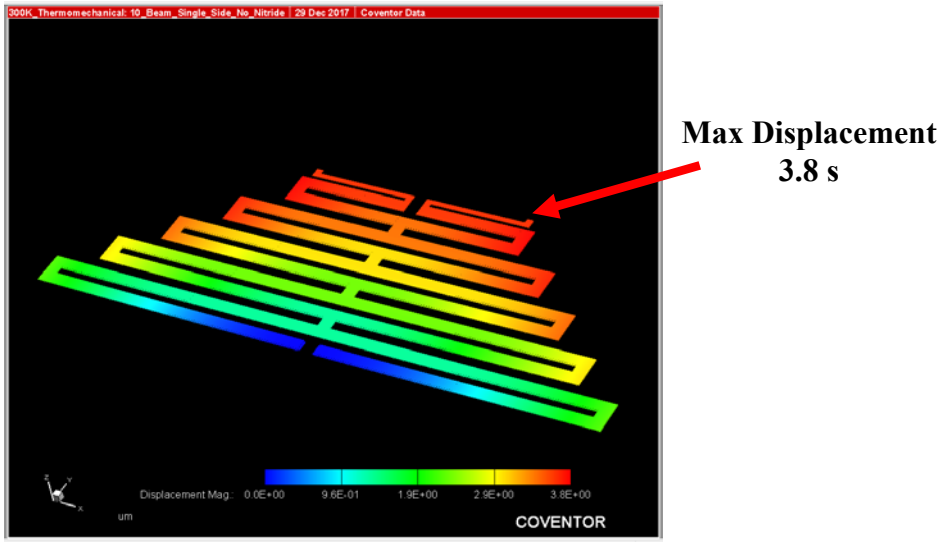

Figure 45:Thermomechanical analysis at 300K for a ten-beam bimorph single side. This does not have the -2GPa nitride layer.

4.3.5 Ten Beam with Nitride

The following thermomechanical, modal harmonic, and electrostatic pull-in analysis (Figure 46-Figure 53: Harmonic response of first mode for ten-beam structure with nitride showing an increase in resonant frequency when three sections of the ten-beam structure are pulled-in.Figure 53) was completed with the AFRL designed ten-beam bimorph beam. The maximum displacement was 490 µm and the resonant frequency for the first harmonic was 2.3 kHz.

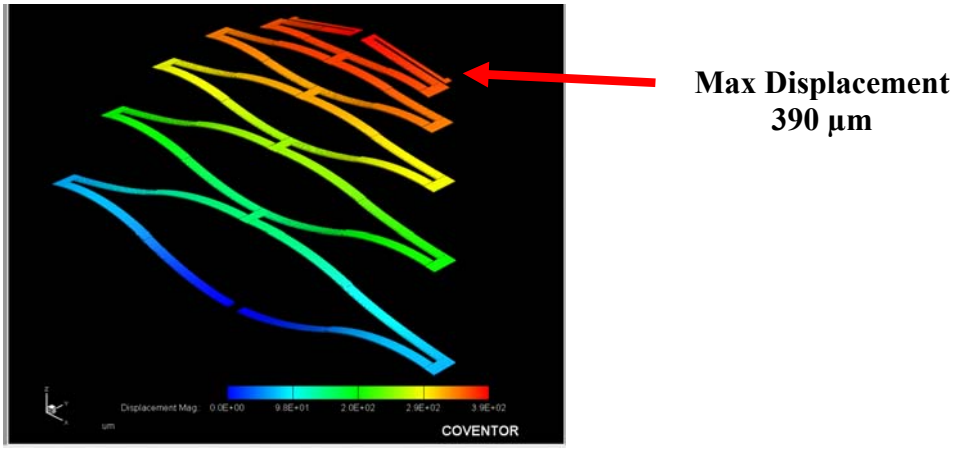

Figure 46: Thermomechanical analysis at 250K for a ten-beam bimorph single side. This does have the -2GPa nitride layer. The displacement is much higher than a comparable analysis performed without the additional nitride layer.

Max Displacement
490 microns

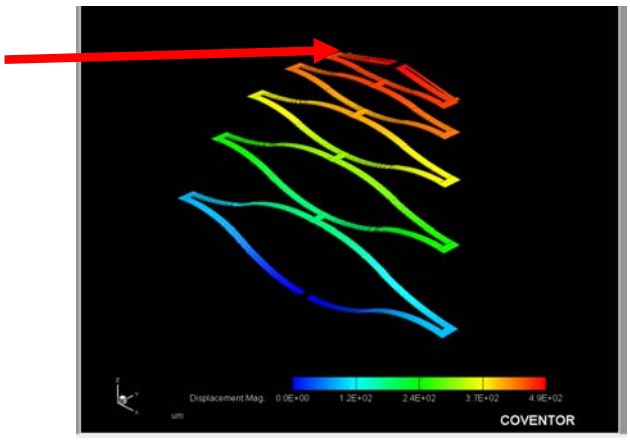

Figure 47: Thermomechanical analysis at 300K for a ten-beam bimorph single side. This does have the -2GPa nitride layer. The displacement is much higher than a comparable analysis performed without the additional nitride layer.

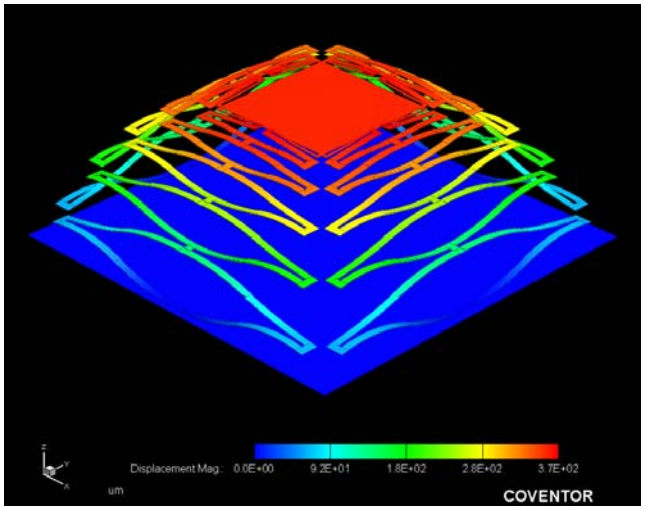

Figure 48: Thermomechanical analysis for a ten-beam bimorph single side. This does have the -2GPa nitride layer. The platform displacement is 370 µm.

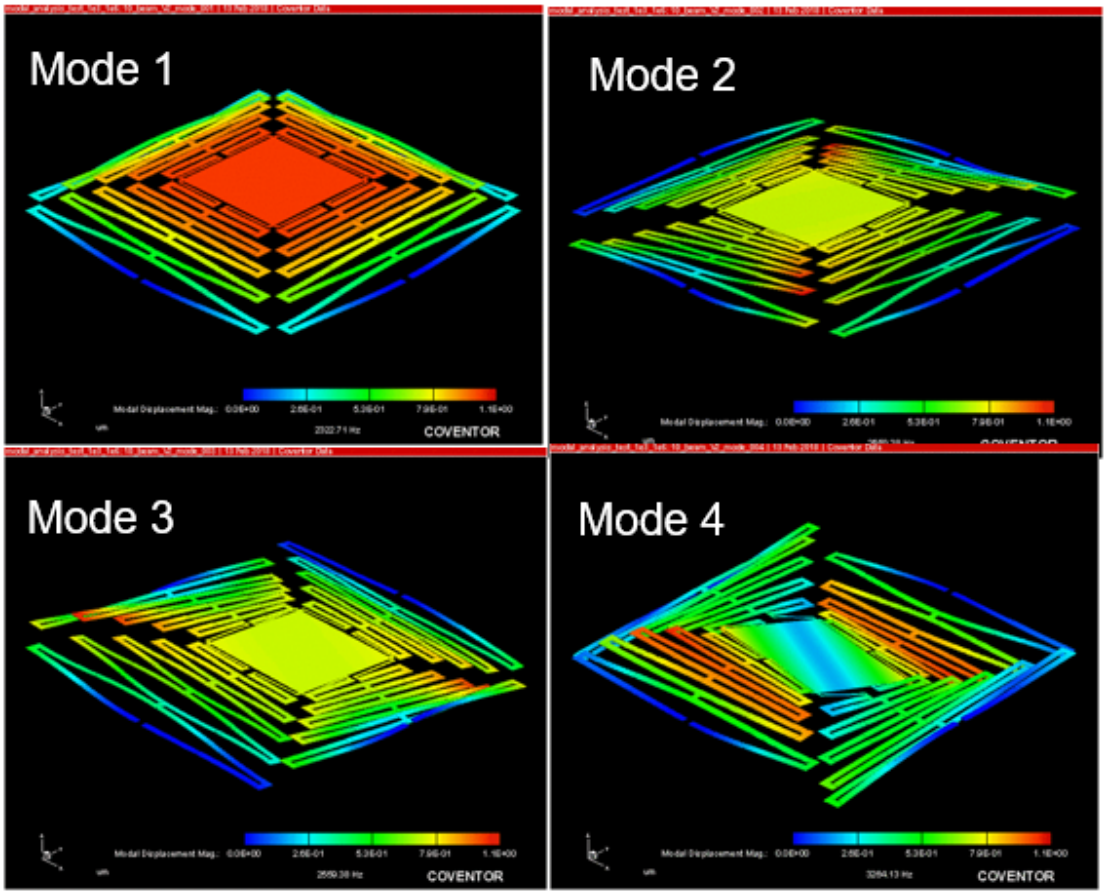

Figure 49: Harmonic modal analysis for ten-beam bimorph. Clockwise from top left, mode 1, 2, 3, and 4. Exaggeration is used to show shapes.

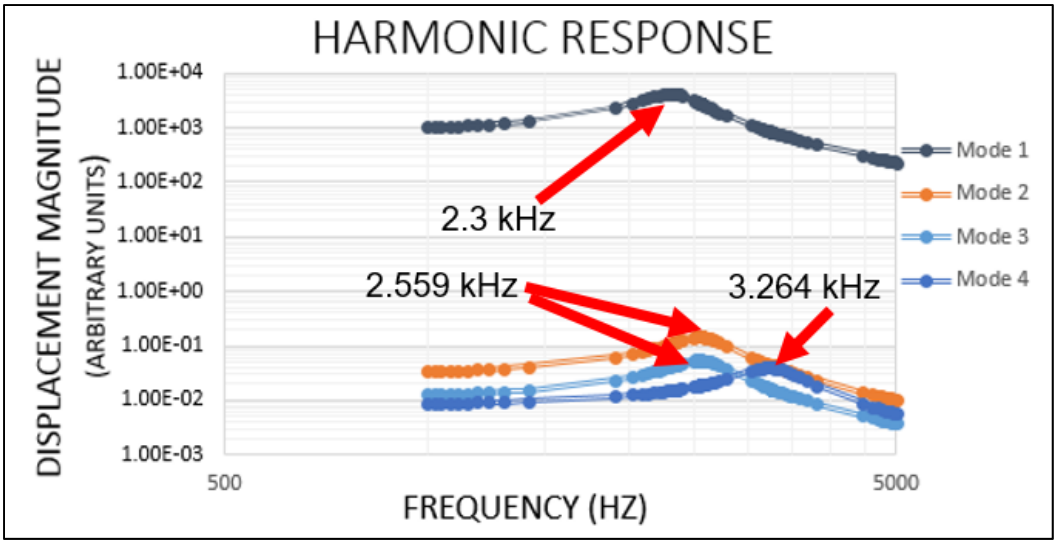

Figure 50: Harmonic response showing spikes at the first four modes of resonant frequency at 2.3 kHz, 2.56kHz, 2.56kHz, and 3.26kHz. This is model of a 10 beam structures with a -2GPa Nitride layer added to increase displacement.

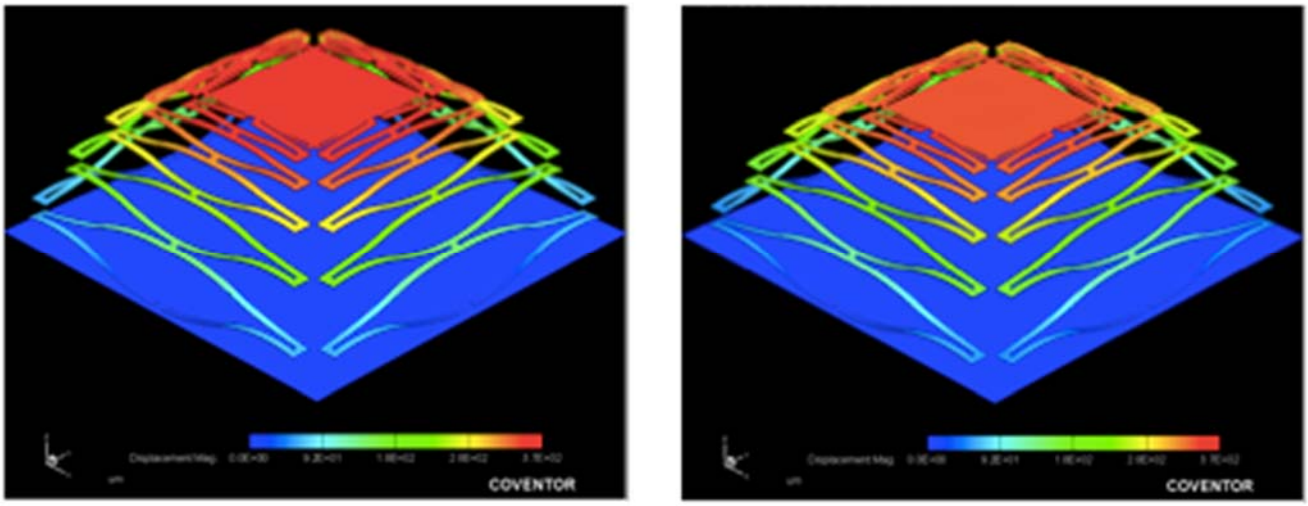

(a) (b)

Figure 51: Electrostatic pull-in analysis for ten-beam with nitride and single large electrode under the structure showing (a) 0V and (b) 316V at point right before pull-in. The maximum displacement at 0V is 355.3 µm and is 335.88 at 316V.

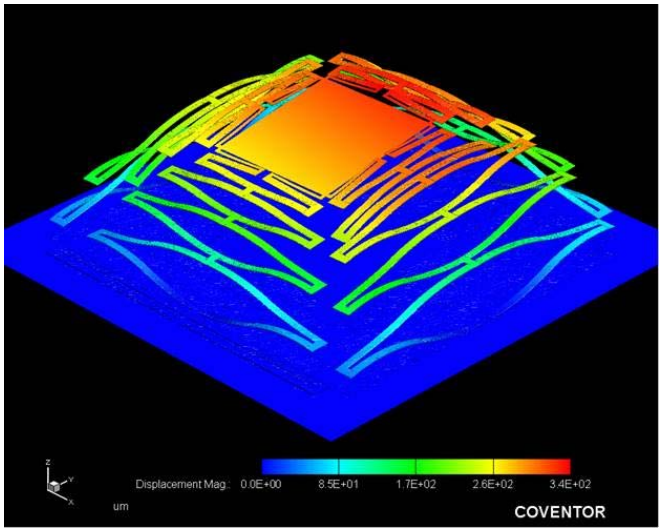

Figure 52: FEA of electrostatic pull-in of segment 3 of a single side of a ten-beam with nitride. Image shows the platform at an angle of 8.89°. The image shown is after the pull-in of segment 2.

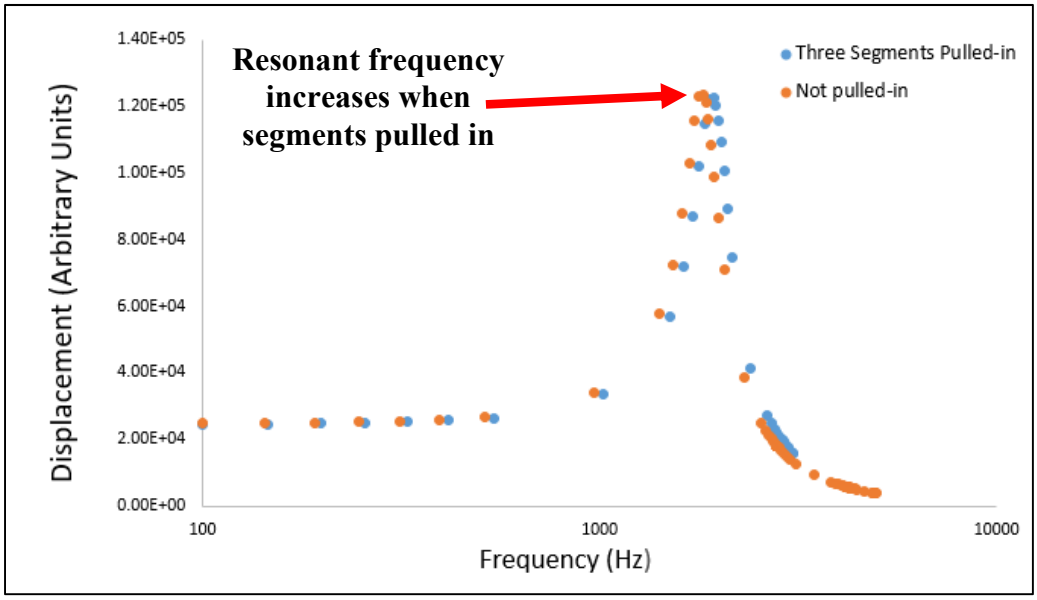

Figure 53: Harmonic response of first mode for ten-beam structure with nitride showing an increase in resonant frequency when three sections of the ten-beam structure are pulled-in.

4.4 Test Results Two Segment Covered

Figure 54 and Table 6 show data from testing of PolyMUMPs devices from run #119.

All measurements were made using released PolyMUMPs devices and used equipment in the

AFIT characterization lab. Measurements to detect the change in capacitance for an actuating electrode were conducted. However, because of limitations on the sensitivity of equipment in the lab, a proper setup to determine the change in capacitance between an non-actuating electrode and the beam structure was not able to be realized. It was found that the attempted setup using a multimeter had a residual capacitance from wiring and equipment of 139 pF which is four orders of magnitude greater than the desired sensitivity for the anticipated change in capacitance of ~10fF. Additional attempts at measuring the change using an oscilloscope and change response to a signal also failed to provide a detectable change in signal. Literature shows that sensors operating in the fF range usually require specially built circuitry to adequately amplify and detect the signal [54].

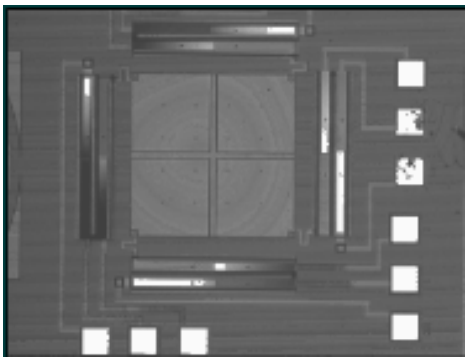

Figure 54: Image of two-beam covered electrode test device using optical microscope of the Zygo white light interferometer.

Table 6: Data measured from applying voltage to (a) electrode 1 and (b) electrode 2 individually and measuring edge of mirror displacement.

Electrode #1 Voltage (V)	Height of Platform (μm)
0	23.60
25	18.60
35	--
50	5.50*

(a)

Electrode #2 Voltage (V)	Height of Platform (μm)
0	22.10
25	20.92
35	20.00
50	17.83

(b)

*Voltage causes pull-in of beam

5. Analysis

The following chapter provides analysis of data collected for this research effort. It compares analytic, FEA, and measured data.

5.1 Two-Beam Segment

The first FEA modeling (Figure 55) that was completed with the two-beam segment. This modeled only a single two-section serpentine bimorph beam. The purpose of this analysis was to provide a proof of concept and guide further research. Analysis of the model as shown in Figure 55 demonstrated that when using literature provided parameters [38] for the dielectric constant for the doped Poly1 layer to model its dielectric behavior, it is possible to individually control each section of the serpentine arms.

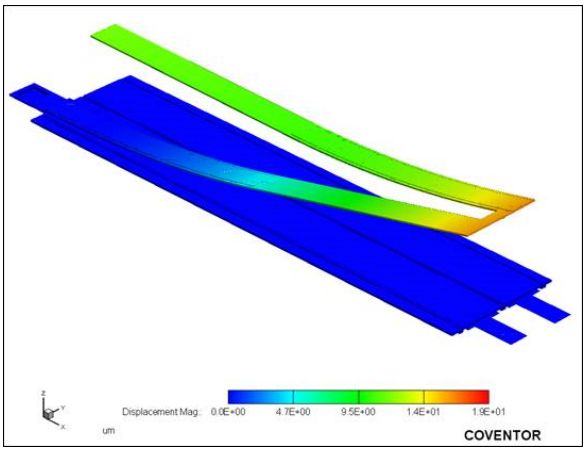

Figure 55: Two-beam individual bimorph beam structure with two independent electrodes made of Poly0 covered by Poly1 layer.

5.2 Analysis of Thermomechanical Modeling

Thermomechanical modeling as shown in Table 7 and Figure 56 showed that as temperature changed, the displacement height of the platform changed. This is expected behavior due to the nature of differential coefficients of thermal expansion present in the

multiple materials of the bimorph beam section. It showed that for both the two-beam structure and the ten-beam structure, a relative minimum for the platform displacement was found around 300K. This may be caused because room temperature residual stress values for the models are input as material parameters because they are process specific. The stress values that were used were provided by the PolyMUMPS foundry and/or by AFRL.

Table 7: Maximum displacement values for a ten-beam with nitride single side showing differential expansion and contraction of the bimorph beams as temperature increases and decreases.

Temperature (K)	Maximum Displacement (μm)
250	390
300	144
350	149

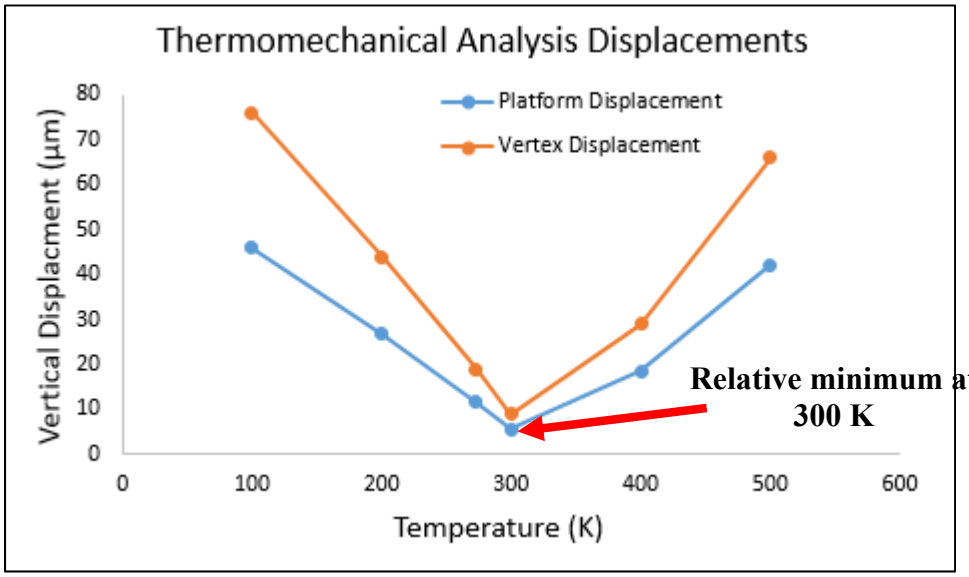

Figure 56: Results for electrothermal FEA modeling showing a relative minimum in vertical displacement for a two-beam structure.

5.3 Modal Analysis

Modal analysis showed the presence of multiple modal harmonics in the kHz range for the modeled devices. As shown in Table 8, comparing different analytic methods wi provide

different anticipated values for the resonant frequency. The Eigen shape method is shown to be a closer proximity to the FEA modeled resonant frequency. Resonant frequency tests of the PolyMUMPs fabricated two-segment structure were not completed. A comparison between the resonant frequency of the two-segment beam structure with and without the addition of the -2GPa nitride layer shows that the resonant frequencies as shown in Table 9.

The ten-beam with nitride structure showed resonant frequency behavior as shown in Figure 50. The anticipated final design of the mirror structure involves the addition of a large post and mirror (Figure 30). The post and mirror add a significant amount of mass (~1.47×10^{-7} kg) to the structure. By using analytical methods of resonant frequency changes with mass and assuming a constant stiffness (k = 0.361 N/m) when the mirror and post is added, the resonant frequency with post and mirror is estimated to be 0.249 kHz (Table 10). The resonant behavior showed an increase for the first mode resonant frequency of 6% when the first three segments of one arm of the ten-beam with nitride was pulled-in indicating an increase in the k value.

Table 8: Comparison of Resonant Frequencies from Analytical Methods and FEA for two-beam structure.

Mode	Simple Harmonic Oscillator $\left(\frac{1}{2\pi}\sqrt{\frac{k}{m}}\right)$	Eigen Shape	FEA
1	300 Hz	1042 Hz	2014 Hz
2	N/A	6534 Hz	3621 Hz
3	N/A	18296 Hz	3651 Hz

Table 9: Comparison of resonant frequencies of two-segment with and without additional -2GPa residual stress nitride layer.

Mode	Two-Beam No Nitride	Two-Beam Nitride
1	2014 Hz	2294 Hz
2	3621 Hz	3798 Hz
3	3651 Hz	3997 Hz

Table 10: Anticipated change in resonant frequency using constant stiffness and change of mass when post and mirror are added to the ten-beam structure.

Model	k (N/m)	Mass (kg)	Frequency (kHz)
Base Structure	0.361	$1.73*10^{-9}$	2.3
Base Structure with Post and Mirror	0.361	$1.47*10^{-7}$	0.249

5.4 Comparison of FEA and measured performance for two-beam

A comparison of the pull-in voltages for single electrode actuation of the two-beam structure shows that the analytic and FEA models provided an underestimate of the pull-in voltage (Table 11). The analytic model may have given an underestimate because the geometry of the beam was simplified to a single cantilever beam. Additionally, the actuation voltage is highly dependent on the height of the cantilever and the analytic model assumes a constant height across the beam. Because of the characteristic curvature of a bimorph beam, the height is not constant and was estimated as the mid-point of the beam for the analytic model. The FEA provided a closer value to the measured pull-in value. Differences in this value can partially be explained by differences in the initial displacement of the platform caused by a larger amount of residual stress caused bimorph displacement. As shown in Figure 57, the initial displacement of the fabricated mirror platform was 24 μm, the anticipated initial displacement of the FEA model mirror platform was 12 μm. This would lead to differences in actuation and pull-in voltages.

Figure 58 and Figure 59 show a comparison of the measured height of the mirror platform structure versus the anticipated height of the displacement mirror platform from an FEA model. As discussed above, the model predicted a much lower initial displacement than was observed by the fabricated device. Because of the difference, normalized values of platform height to the initial platform height are provided in Figure 60 and Figure 61. As expected, the

general shape of the measured and anticipated are similar. Both lines decrease as voltage increases and accelerate in the rate of decrease as pull-in voltage is approached.

Table 11: Comparison of pull-in voltages for analytic, FEA, and measured values for two-beam covered electrode structure. All values are for single electrode actuation.

Model	Analytic (V)	FEA (V)	Measured (V)
Electrode 1	14.7	21.6	25-50
Electrode 2	41.6	35.6	>50

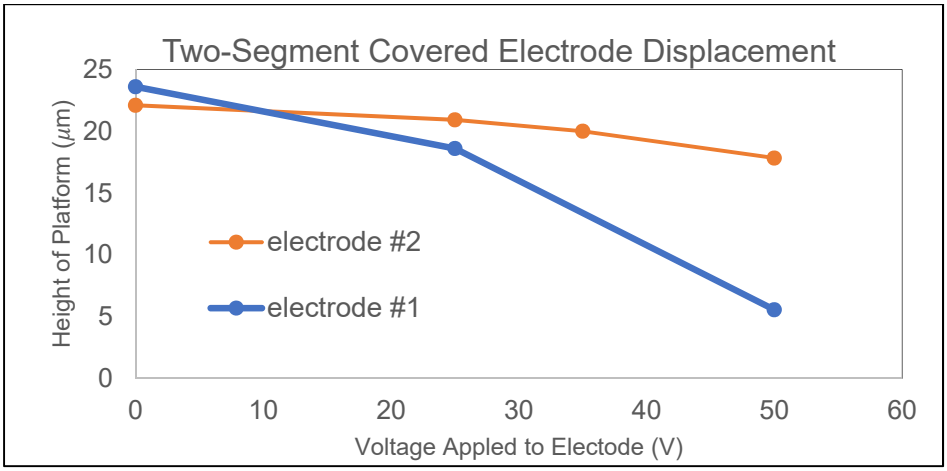

Figure 57: Plot of height of platform for a two-segment covered electrode mirror as a voltage is applied to electrode 1 and electrode 2.

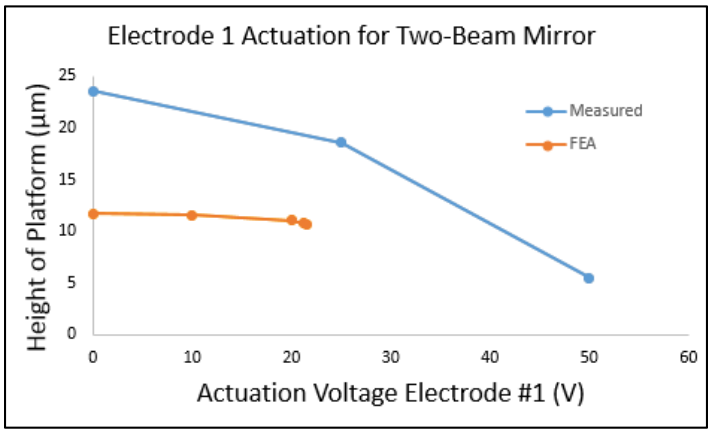

Figure 58: Comparison of measured and FEA data for electrode 1 actuation for two-segment mirror.

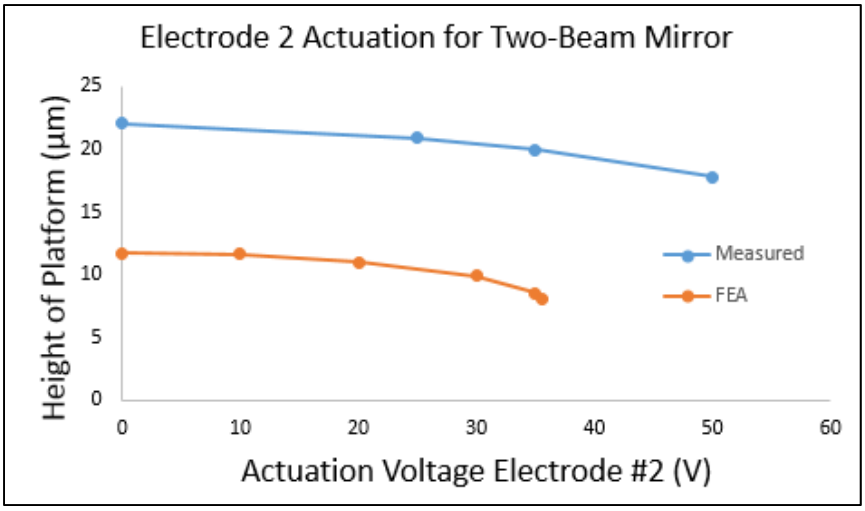

Figure 59: Comparison of measured and FEA data for electrode 2 actuation for two-segment mirror.

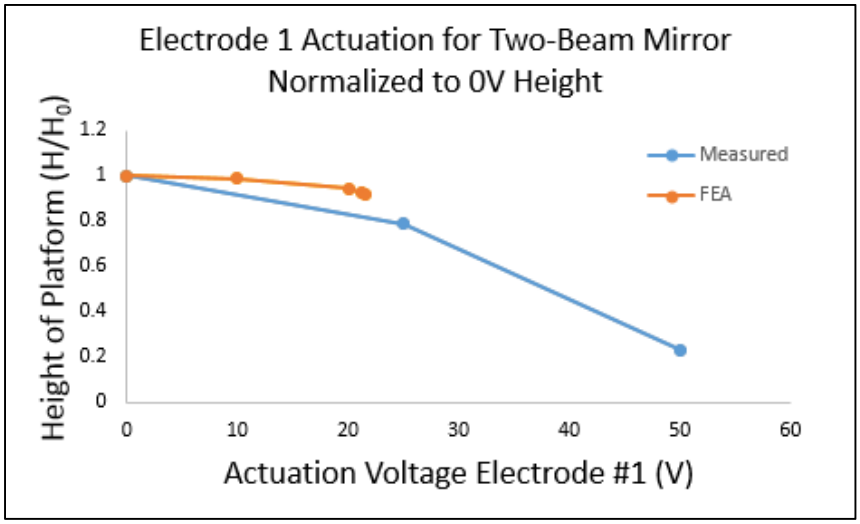

Figure 60: Comparison of measured and FEA normalized data for electrode 1 actuation for two-segment mirror.

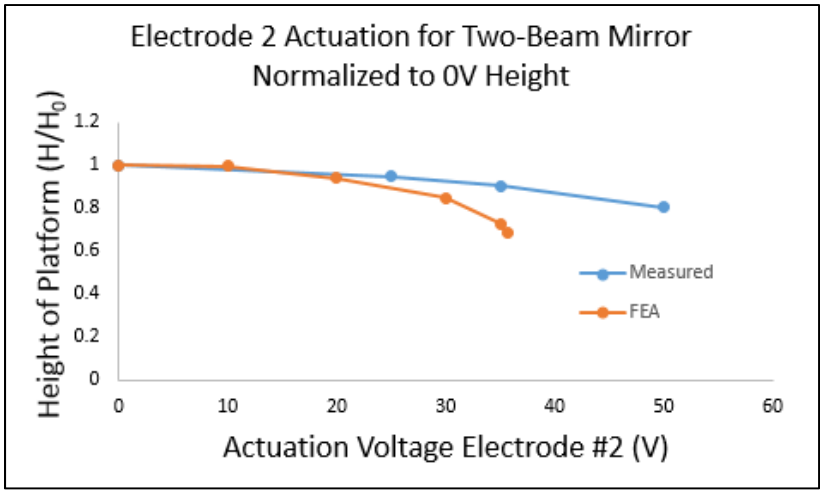

Figure 61: Comparison of measured and FEA normalized data for electrode 2 actuation for two-segment mirror.

5.5 Comparison of Actuation with Different Actuation Excitement Schemes

As shown in Figure 62, the behavior of the actuation of the beam varies depending on which electrodes are being used to apply the actuating voltages. The initial deflections are similar, however the pull-in voltages are different for electrode #1 and #2.. The anticipated function would be to apply a voltage electrode #1 until pull-in is reached, at that point, begin applying a voltage to electrode #2 until pull-in is reached for electrode #2. If additional segments are available, continue until all electrodes have been pulled-in. Figure 62 shows that by simultaneously actuating electrodes on multiple sides, actuation is also possible. This is advantageous because it provides a rotation of the platform about a different axis than a single side actuation.

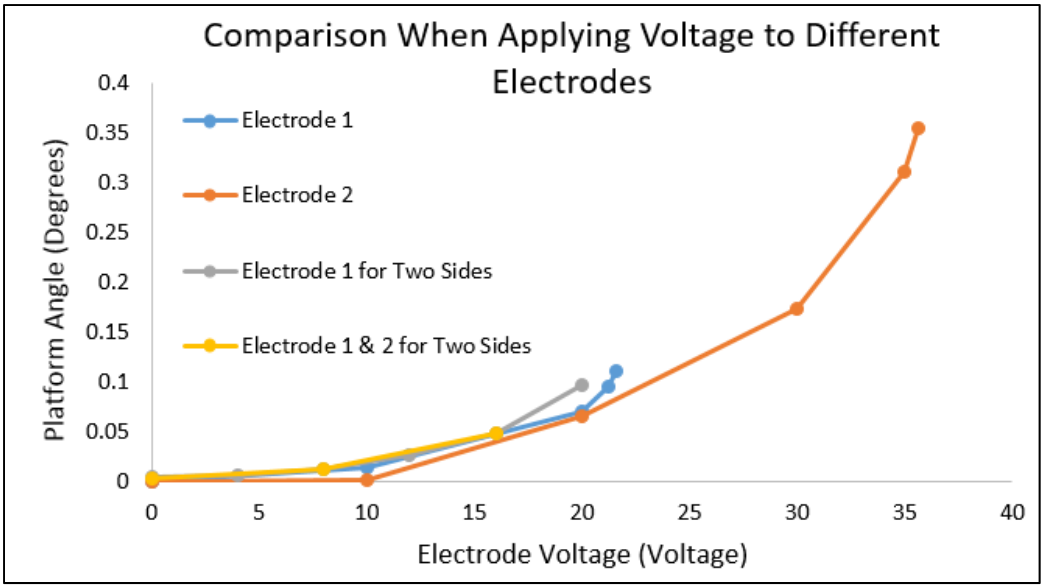

Figure 62: Comparison of different application schemes of voltages and effects to platform deflection.

Pull-in analysis of the ten-beam nitride structure (Figure 63) showed a required pull-in voltage of 316 V for a single large electrode. This pull-in is for a single large electrode under the entire beam structure. According to this analysis, the pull-in occurs when the platform is at a height of 336 µm. This is not much lower than the maximum height of 355 µm. With a single electrode, this provides stable solutions to just 5.4% of the full displacement of the beam structure. When a segmented electrode approach is used as shown in Figure 64 and Figure 65, this adds additional intermediate states for both displacement and angular deflection. Each of the intermediate steps adds a small amount of stable displacement values.

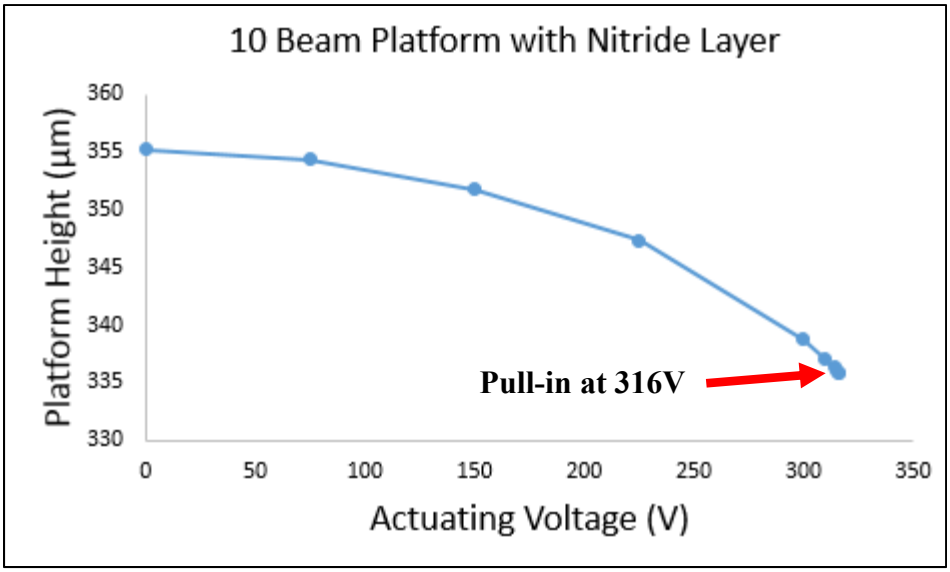

Figure 63: Plot of electrostatic pull-in analysis for ten-beam with nitride and single large electrode under the structure

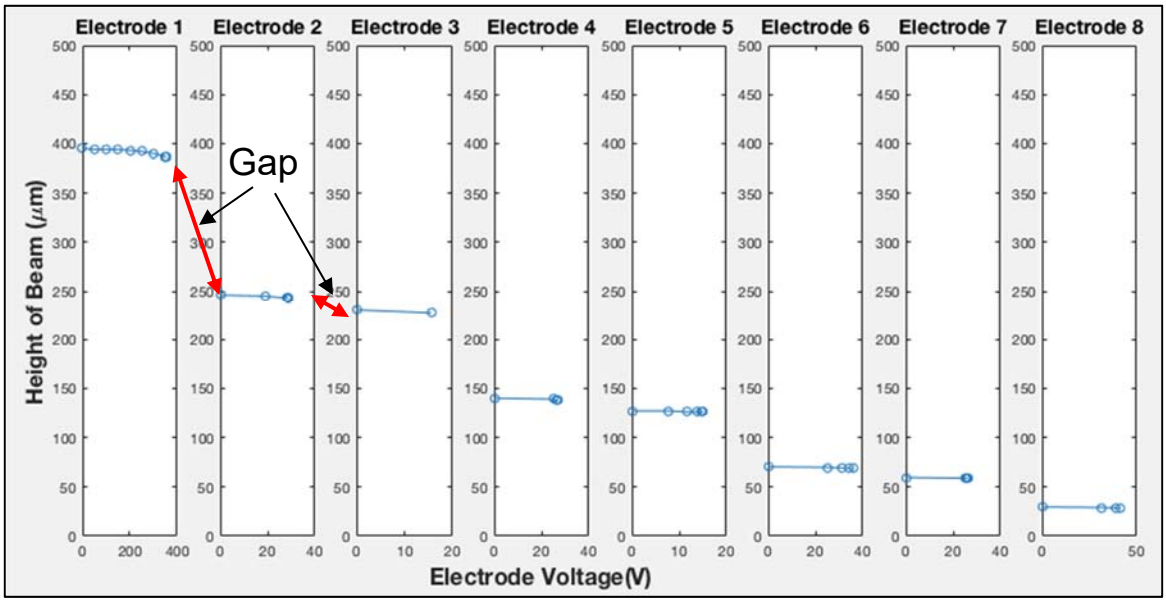

Figure 64: FEA pull-in analysis for a single ten-beam with nitride using ten segmented electrodes. This plot shows gaps between the static stable displacement regions after each segment pull-in.

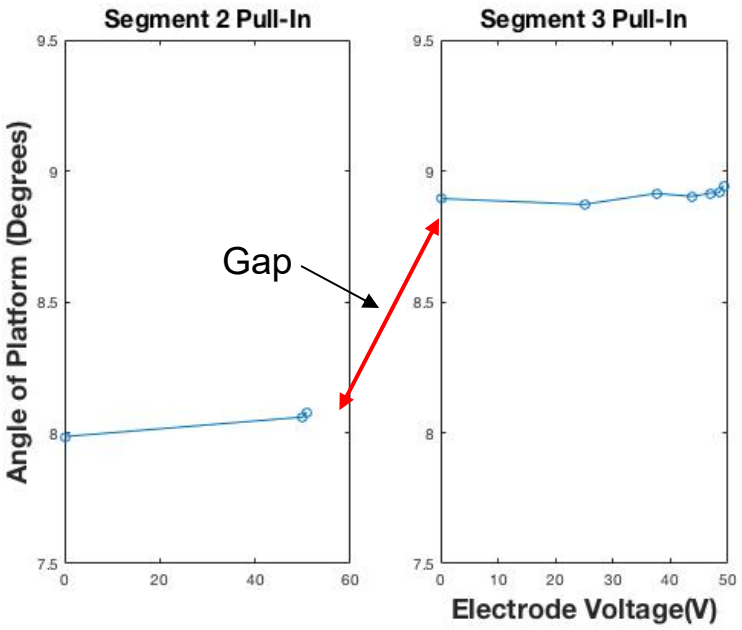

Figure 65: FEA pull-in analysis for the ten-beam with nitride. This plot shows additional stable angular deflections states are added during the pull-in of additional electrodes.

5.6 Capacitive actuation sensing.

The model as shown in Figure 55 was used to determine the feasibility of using only some electrodes for actuation and using other electrodes to measure the beam structure displacement through variable capacitive sensing. The intention is that the signal from the variable capacitive sensing could then be used for a closed-loop controller to accurately control mirror vertical and angular displacement. As shown in Figure 66, the FEA modeling shows that change in capacitance is measurable between the non-actuating electrode and the beam. The change in capacitance is very small and as shown is in the fF range. This small level of capacitance change is challenging to measure. However, there are currently available sensors that operate in the fF range and circuitry is available to detect such a small signal [55].

Additionally, FEA shows that the closer electrode (electrode #1) creates a greater change in capacitance per change in vertex height or in other words, it is more sensitive.

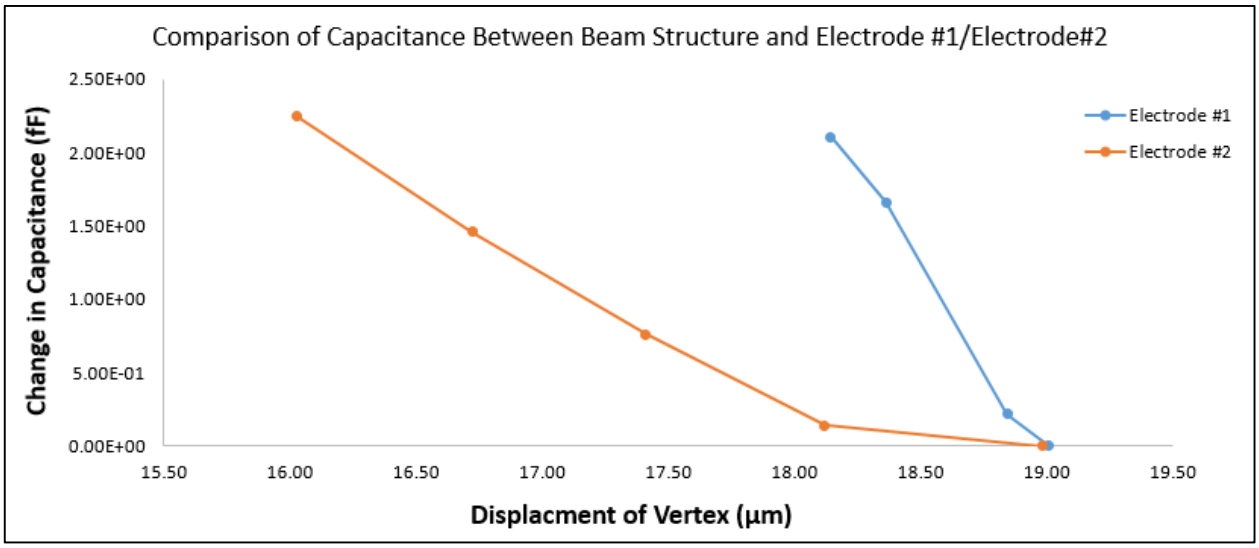

Figure 66: Plot of FEA model results for the change in capacitance between each electrode and the beam on the vertical axis and the change in the vertex height on the horizontal axis. This shows a measureable change in capacitance as the vertical displacement of a beam changes.

5.7 Summary

In summary, analytic modeling, FEA simulation and prototype measuring were used to demonstrate and characterize methods for controlling an electrostatic bimorph beam structure through segmented electrodes. Analysis looked at proof-of-concept, thermomechanical modeling, harmonic responses, pull-in and electrostatic deflection behavior. Analytic modeling and FEA simulation showed anticipated performance and lab measurement of a prototype demonstrate real performance of segmented control schemes.

6. Conclusions and Recommendations

6.1 Conclusion of Research

The work provided in this thesis provides a summary of background, methodology, design, modeling, fabrication, and testing of a novel control scheme for segmented control of electrostatically actuated bimorph beam structures (Figure 67). The first analysis showed a proof-of-concept for the design and further analysis showed the anticipated performance and behavior of such control structures, and finally, the prototype demonstration demonstrated the basic functionality of the device.

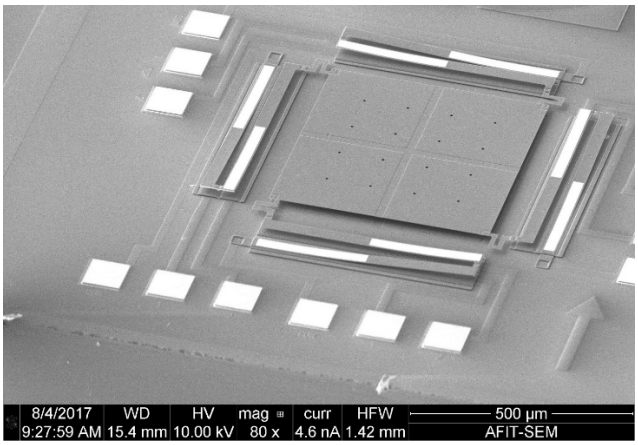

Figure 67: SEM of released PolyMUMPS fabricated two-beam micromirror structure.

6.2 Significance of Research

This research looked at improving the current state of the art for electrostatically actuated bimorph micro arrays. The following main conclusions were found.

6.2.1 Resonant modal analysis of structures

FEA resonant modal analysis showed that by increasing the displacement of the beam structure by adding the nitride layer, the resonant frequency of the device increased. Additionally, theory and FEA analysis show that the anticipated change first mode harmonic

frequency for the ten-segment beam structure should change from 2.3 kHz to 0.249 kHz when the post and mirror are added to the central beam structure. This large change could be offset by reducing the mass of the post and mirror. Finally, when segments were pulled-in, the resonant frequency of the structure increased indicating a stiffening of the k value.

6.2.2 Segmented electrode architecture effect on pull-in

FEA and prototype testing showed that the pull-in behavior is different for the different electrodes. In other words, the pull-in voltage and pull-in displacement for electrode 1 is not the same as the pull-in voltage and pull-in displacement for when electrode 2. This was shown increase the range of available static stable angular and vertical displacement solutions for the micromirror platform.

6.2.3 Function in capacitive sensing mode

FEA analysis indicates that use of individual electrodes as a variable capacitor to detect the displacement of the beam structure is a feasible design. Modeling indicates that the change in capacitive to be on the order of fF. This is quite small, but may be able to be used as a measurement signal for a closed loop control system. The use of the segmented design for change in capacitance was unable to be demonstrated in the lab using the prototype because of limitations to detect such a small change in capacitance.

6.3 Recommendations for Future Research

To continue this research effort, demonstration of segmented control beyond a two-segment prototype device should be shown. Included in this thesis are descriptions and L-edit design of such devices. Future research should focus on finding the expanded range of possible static stable displacement solutions and work to minimize any unstable regions. Additionally, as

discussed in the methodology section, an alternative design that uses posts instead of fully covered electrode pads may show additional benefits and should be researched.

To be able to feasibly use the segmented electrodes in capacitive sensing mode, an entire closed loop feedback control and capacitance measurement circuitry would need to be designed and implemented. This could be more of a final last step before implementation of a micromirror array.

6.4 Summary

In conclusion, this thesis presented analytical, FEA modeling, and prototype testing of a segmented control of electrostatically actuated bimorph beam for use in a micromirror array. This research found that the pull-in and displacement behavior of a bimorph beam changes as the electrode configuration changes and that this could increase the range of static stable solutions for beam structure displacement.

Appendix A. PolyMUMPS Run Data

The following data tables (Table 12 and Table 13) are the measured material properties from PolyMUMPs run 119 and run 121.

Table 12: Material properties measured from PolyMUMPs run 119.

Lot 11989 Run119	Thickness (A)	Deviation (A)	Sheet Resistance (ohm/sq)	Resistivity (ohm-cm)	Stress (MPa)	
Nitride	5921	183.87			89	(T)
Poly 0	5019	30.15		#VALUE!	-3	c
Oxide 1	19691	214.10				
Poly 1	19886	82.45		#VALUE!	-9	c
Oxide 2	7322	113.64				
Poly 2	14886	76.33		#VALUE!	-12	c
Metal	4920				16	(T)

Table 13: Material properties measured from PolyMUMPs run 121

Lot 12048 Run121	Thickness (A)	Deviation (A)	Sheet Resistance (ohm/sq)	Resistivity (ohm-cm)	Stress (MPa)	
Nitride	6166	208.50			64	(T)
Poly 0	5031	28.76			-15	c
Oxide 1	19507	365.33				
Poly 1	20055	101.18			-11	c
Oxide 2	7515	98.21				
Poly 2	15023	69.17			-13	c
Metal	5160		0.060		18	(T)

Appendix B. Additional Background on Doping

One of the properties of semiconductors that make it extremely useful for microelectronics and MEMS is the ability to change the electronic band structure of the material through doping. Doping is done through adding impurities into the crystal structure to add either additional electrons or holes (absences of electrons); the former is called N-type and the latter is called P-type. By adjusting the level of holes and electrons, the fermi level can be adjusted. This is extremely useful for the design of many microelectronic components such as diodes. Two important properties for MEMS devices that doping is able to change is the resistivity and dielectric constant of a material [16], [38]. Resistivity is the measurement of a materials ability to resist electrical conductivity. It is usually measured in units of ohm/centimeters (Ω/m). Metals and other conductors typically have a small resistivity while semiconductors and insulators have larger levels of resistivity [56]. Figure 68 shows the relationship for crystalline silicon between the resistivity and the dopant density.

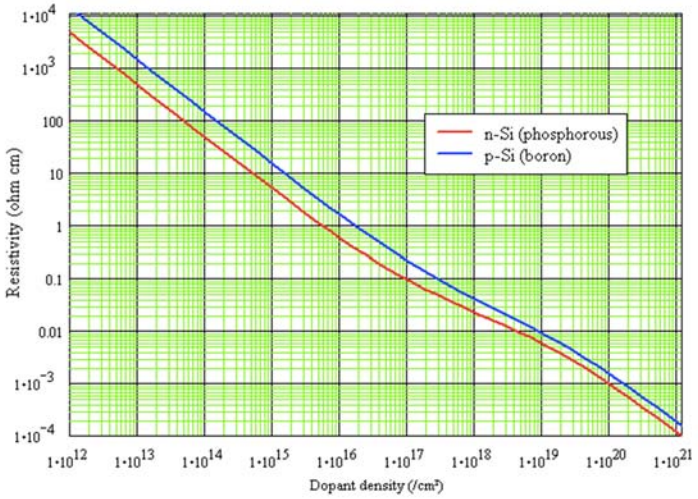

Figure 68: Resistivity for silicon as a function of N and P type dopants [56].

In addition to the resistivity, doping has an effect on the dielectric constant.

The dielectric constant is the ratio of the relative permittivity of a material to the permittivity of a vacuum. To change the dielectric constant, for silicon in particular the addition of donor atoms (N_D) will increase the dielectric constant from its undoped (intrinsic) value. Equation (30) provides a relationship for n-type doping of silicon at room temperature using phosphorous [38].

$$\epsilon_r(N_D) = 11.688 + 1.635 * \frac{10^{-19} N_D}{1 + 1.172 * 10^{-21} N_D} \tag{30}$$

Appendix C. Additional Information for Analytical Work

Figure 69: Calculation of (k) for two-segment design

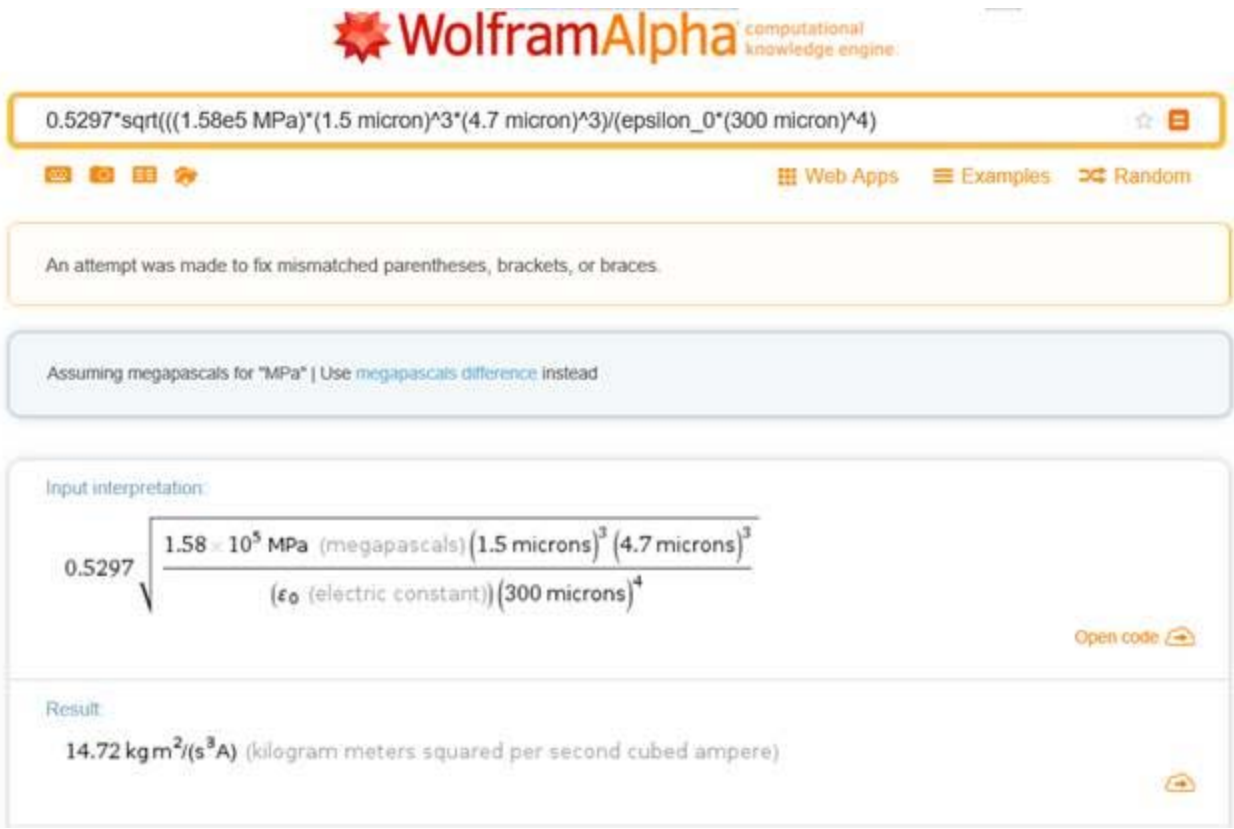

Figure 70: Calculation of stiffness V_{pi} for Electrode 1.

BIBLIOGRAPHY

[1] K. B. Lee, *Principles of Microelectromechanical Systems*. John Wiley & Sons, Inc, 2011.

[2] R. Feynman, "There's plenty of room at the bottom," *Australasian Biotechnology*, vol. 16, no. 3. p. 36, 2006.

[3] V. Cahill, "Inkjet Printhead Developments," no. December, pp. 21–30, 2016.

[4] H. Fujita, "A decade of MEMS and its future," *Proc. IEEE Tenth Annu. Int. Work. Micro Electro Mech. Syst. An Investig. Micro Struct. Sensors, Actuators, Mach. Robot.*, pp. 1–7, 1997.

[5] R. Ernst, Peter, Bosch, "MEMS @ BOSCH: Automotive applications and beyond," *Automotive Electronics*.

[6] R. Station, "A National Historic Mechanical Engineering Landmark," *Am. Soc. Mech.*, 1983.

[7] A. Kheyraddini Mousavi and Z. C. Leseman, "Basic MEMS Actuators," in *Encyclopedia of Nanotechnology*, B. Bhushan, Ed. Dordrecht: Springer Netherlands, 2012, pp. 173–185.

[8] M. Vladimer, "Sensors, Actuators and IoT," *LinkedIn*, 2015. [Online]. Available: https://www.linkedin.com/pulse/sensors-actuators-iot-mike-vladimer/.

[9] R. . Adams, T.M., Layton, *MEMS transducers—An overview of how they work.* Boston, MA: Springer, 2010.

[10] P. J. French, "Development of surface micromachining techniques compatible with on-chip electronics," *J. Micromechanics Microengineering*, vol. 6, pp. 197–211, 1999.

[11] A. Utz, C. Walk, A. Stanitzki, M. Mokhtari, M. Kraft, and R. Kokozinski, "A high precision MEMS based capacitive accelerometer for seismic measurements," pp. 3–5,

2017.

[12] S. Lloyd and M. Lim, “The Age of Sensors – How MEMS sensors will enable the next wave of new products .,” 2016.

[13] M. Gad-el-Hak, *The MEMS Handbook*. CRC Press LLC, 2002.

[14] K. C. Schadow, “Introduction,” no. October 2002, pp. 27–28, 2003.

[15] I. V Uvarov, V. V Naumov, P. Podder, and P. Constantinou, “Microelectromechanical systems (MEMS): fabrication , design and,” vol. 10, pp. 1115–1134, 2001.

[16] K. N. Sze, S.M., Kwok, *Physics of Semiconductor Devices*, 3rd ed. 2007.

[17] “Semiconductor Technology from A to Z,” *Hal Bleiter*. [Online]. Available: https://www.halbleiter.org/en/fundamentals/conductors-insulators-semiconductors/. [Accessed: 18-Jan-2018].

[18] D. Koester, A. Cowen, and R. Mahadevan, “PolyMUMPs design handbook,” *MEMSCAP Inc*, 2013.

[19] N. Ashcroft, N, Mermin, *Solid State Physics*. Saunders, 1976.

[20] H. C. Card and E. S. Yang, “Electronic processes at grain boundaries in polycrystalline semiconductors under optical illumination,” *IEEE Trans. Electron Devices*, vol. ED-24, pp. 397–402, 1977.

[21] B. El-Kareh, *Fundamental of Semiconductor Processing Technologies*. Norwell: Kluwer Academic Publishers, 1995.

[22] T.-R. Hsu, *MEMS and Microsystems*. Hoboken, NJ: John Wiley & Sons, Inc, 2008.

[23] S. Campbell, *Fabrication Engineering*, Fourth. New York, NY: Oxford University Press, 2013.

[24] H. R. Khaleel, H. M. Al-Rizzo, and A. I. Abbosh, “Design, Fabrication, and Testing of

Flexible Antennas," in *Advancement in Microstrip Antennas with Recent Applications*, A. Kishk, Ed. Rijeka: InTech, 2013.

[25] D. Liu and W. (Will Shu, "Microcantilever Biosensors: Probing Biomolecular Interactions at the Nanoscale," *Curr. Org. Chem.*, vol. 15, pp. 477–485, 2011.

[26] D. A. Jameel, "Thin Film Deposition Processes," *Int. J. Mod. Phys. Appl.*, vol. 1, no. 4, pp. 193–199, 2015.

[27] "No Title," *ECS J. Solid State Sci. Technol.*

[28] "Plasma Enhanced Chemical Vapor Deposition," *LNF University of Michigan WIKI*. [Online]. Available: http://lnf-wiki.eecs.umich.edu/wiki/Plasma_enhanced_chemical_vapor_deposition. [Accessed: 18-Feb-2018].

[29] G. T. A. Kovacs, N. I. Maluf, and K. E. Petersen, "Bulk micromachining of silicon," *Proc. IEEE*, vol. 86, no. 8, pp. 1536–1551, 1998.

[30] F. Karouta, "A practical approach to reactive ion etching," *J. Phys. D. Appl. Phys.*, vol. 47, no. 23, p. 233501, Jun. 2014.

[31] "Background material on reactive ion etching," *Rensellear Polytechnic Institute: SCOREC Scientific Computation Research Center*. [Online]. Available: https://scorec.rpi.edu/research_plasmaetchmodeling.php.

[32] "PolyMUMPs," *MEMSCAP Inc*. [Online]. Available: http://www.memscap.com/products/mumps/polymumps. [Accessed: 17-Feb-2017].

[33] R. D. Gerke, "CH: 8 MEMS Packaging." .

[34] "MEMS Packaging," *Washington State University: Center for Materials Research*. .

[35] H. Xie, "Advanced MEMS."

[36] S. Wang, Y. Hao, and S. Liu, “The design and analysis of a MEMS electrothermal actuator,” *J. Semicond.*, vol. 36, no. 4, 2015.

[37] H. Fangohr, D. S. Chernyshenko, M. Franchin, T. Fischbacher, and G. Meier, “Joule heating in nanowires,” *Phys. Rev. B - Condens. Matter Mater. Phys.*, vol. 84, no. 5, pp. 1–14, 2011.

[38] S. Ristic, A. Prijic, and Z. Prijic, “Dependence of static dielectric constant of silicon on resistivity at room temperature,” *Serbian J. Electr. Eng.*, vol. 1, no. 2, pp. 237–247, 2004.

[39] Y.-H. Lim, V. V Varadan, and V. K. Varadan, “Finite-element modeling of the transient response of MEMS sensors,” *Smart Mater. Struct.*, vol. 6, no. 1, pp. 53–61, Feb. 1997.

[40] U. of T. Arlington, “Mechanical Properties of Materials.” [Online]. Available: http://wweb.uta.edu/faculty/ricard/Classes/KINE-3301/Notes/Lesson-14.html. [Accessed: 17-Nov-2017].

[41] S. M. Heinrich and I. Dufour, “Fundamental Theory of Resonant MEMS Devices,” *Reson. MEMS Princ. Model. Implementation, Appl.*, pp. 1–28, 2015.

[42] A. Bounouh and D. Bélières, “Resonant frequency characterization of MEMS based energy harvesters by harmonic sampling analysis method,” *Meas. J. Int. Meas. Confed.*, vol. 52, no. 1, pp. 71–76, 2014.

[43] W. M. Zhang, H. Yan, Z. K. Peng, and G. Meng, “Electrostatic pull-in instability in MEMS/NEMS: A review,” *Sensors Actuators, A Phys.*, vol. 214, pp. 187–218, 2014.

[44] Y. Sun, D. Piyabongkarn, A. Sezen, B. J. Nelson, and R. Rajamani, “A high-aspect-ratio two-axis electrostatic microactuator with extended travel range,” *Sensors Actuators, A Phys.*, vol. 102, no. 1–2, pp. 49–60, 2002.

[45] Z. Changfu, J. Zhuangde, L. Dejiang, and R. Taian, “3D MEMS design method via

SolidWorks," *Proc. 1st IEEE Int. Conf. Nano Micro Eng. Mol. Syst. 1st IEEE-NEMS*, pp. 747–751, 2006.

[46] H.-H. Lee, *Finite Element Simulations with ANSYS Workbench 17*. SDC Publications, 2017.

[47] M. R. Douglass, "MEMS reliability: coming of age," vol. 688402, no. February 2008, p. 688402, 2008.

[48] K. S. Lim and J. B. Yoon, "Stepwise Actuation of an Electrostatic Bimorph Cantilever Actuator Using a Patterned Bottom Electrode," *J. Microelectromechanical Syst.*, vol. 25, no. 5, pp. 909–915, 2016.

[49] J. P. Walton, R. A. Coutu Jr., and L. Starman, "Modeling and simulations of new electrostatically driven, bimorph actuator for high beam steering micromirror deflection angles," *MOEMS Miniaturized Syst. XIV*, vol. 9375, p. 93750Y, 2015.

[50] John P.K. Walton, "Electrostatically Driven Large Aperture Micro-Mirror Actuator Assemblies for High Fill-Factor, Agile Optical Phase Arrays," Air Force Institute of Technology, Wright-Patterson AFB, OH, 2015.

[51] L. Starman, J. Walton, H. Hall, and R. Lake, "Post Fabrication Processing of Foundry MEMS Structures Exhibiting Large, Out-of-Plane Deflections," *Proceedings*, vol. 1, no. 5, p. 553, 2017.

[52] I. W. Jung, S. Member, U. Krishnamoorthy, and O. Solgaard, "High Fill-Factor Two-Axis Gimbaled Tip-Tilt-Piston Micromirror Array Actuated by Self-Aligned Vertical Electrostatic Combdrives," vol. 15, no. 3, pp. 563–571, 2006.

[53] S. Waldis, F. Zamkotsian, P. A. Clerc, W. Noell, M. Zickar, and N. De Rooij, "Arrays of high tilt-angle micromirrors for multiobject spectroscopy," *IEEE J. Sel. Top. Quantum*

Electron., vol. 13, no. 2, pp. 168–175, 2007.

[54] J. Wei, C. Yue, Z. L. Chen, Z. W. Liu, and P. M. Sarro, "A silicon MEMS structure for characterization of femto-farad-level capacitive sensors with lock-in architecture," *J. Micromechanics Microengineering*, vol. 20, no. 6, p. 64019, 2010.

[55] A. Tanskanen, B. Bahreyni, and M. Syrzycki, "Charge-based femto-farad capacitance measurement technique for MEMS applications," *Can. Conf. Electr. Comput. Eng.*, vol. 2016–Octob, no. 1, 2016.

[56] Thurber, Mattis, Liu, and Filliben, "The Relationship Between Resistivity and Dopant Density for Phosphorus- and Boron-Doped Silicon." U.S. Department of Commerce National Bureau of Standards, 1981.

REPORT DOCUMENTATION PAGE

Form Approved
OMB No. 074-0188

PLEASE DO NOT RETURN YOUR FORM TO THE ABOVE ADDRESS.

1. REPORT DATE *(DD-MM-YYYY)*	**2. REPORT TYPE**	**3. DATES COVERED** *(From – To)*
22-03-2018	Master's Thesis	August 2016 – March 2018

TITLE AND SUBTITLE

Segmented Control of Electrostatically Actuated Bimorph Micromirrors

5a. CONTRACT NUMBER

5b. GRANT NUMBER

5c. PROGRAM ELEMENT NUMBER

6. AUTHOR(S)

Waggoner, Kullen W., Captain, USAF

5d. PROJECT NUMBER

5e. TASK NUMBER

5f. WORK UNIT NUMBER

7. PERFORMING ORGANIZATION NAMES(S) AND ADDRESS(S)

Air Force Institute of Technology
Graduate School of Engineering and Management (AFIT/EN)
2950 Hobson Way, Building 640
WPAFB OH 45433-8865

8. PERFORMING ORGANIZATION REPORT NUMBER

AFIT-ENG-MS-18-M-065

9. SPONSORING/MONITORING AGENCY NAME(S) AND ADDRESS(ES)

Intentionally left blank

10. SPONSOR/MONITOR'S ACRONYM(S)

11. SPONSOR/MONITOR'S REPORT NUMBER(S)

12. DISTRIBUTION/AVAILABILITY STATEMENT

DISTRUBTION STATEMENT A. APPROVED FOR PUBLIC RELEASE; DISTRIBUTION UNLIMITED.

13. SUPPLEMENTARY NOTES

14. ABSTRACT

Electrostatic actuating bimorph beams are a MEMS device that can be used to control arrays of small micromirrors for optical scanning. Previous research has demonstrated that creating high-angle deflection using long repeating arms of bimorph beams is possible. The current devices lack precise control and measurement of the mirror deflection. A solution to improve control and measurement by using segmented bias channels to control separate portions of the actuation arm. The amount of mirror deflection will vary depending on which segments of the arm are actuated. This poster discusses the results of FEA modeling and testing.

15. SUBJECT TERMS

micro-mirror array, beam steering, electrostatic, high deflection, segmented control

16. SECURITY CLASSIFICATION OF:			**17. LIMITATION OF ABSTRACT**	**18. NUMBER OF PAGES**	**19a. NAME OF RESPONSIBLE PERSON**
a. REPORT	**b. ABSTRACT**	**c. THIS PAGE**			Robert A. Lake, Captain, PhD, USAF AFIT/ENG
U	**U**	**U**	**UU**	104	**19b. TELEPHONE NUMBER** *(Include area code)* (937) 255-3636 (x4550) (robert.lake@afit.edu)

Standard Form 298 (Rev. 8-98)
Prescribed by ANSI Std. Z39-18